Diploma thesis

Characterization of CrN films on MgO by Transmission Electron Microscopy

Karoline Sophie Kormout

Montanuniversität Leoben

Department Material Physics

and Erich Schmid Institute of Material Science,

Austrian Academy of Sciences

EIDESSTATTLICHE ERKLÄRUNG

Ich erkläre an Eides statt, dass ich diese Arbeit selbstständig verfasst, andere als die angegebenen Quellen und Hilfsmittel nicht benutzt und mich auch sonst keiner unerlaubten Hilfsmittel bedient habe.

AFFIDAVIT

I declare in lieu of oath, that I wrote this thesis and performed the associated research myself, using only literature cited in this volume.

Leoben, June 2012 Karoline Kormout

Abstract

The microstructure of two CrN thin films and their interface with an MgO substrate were investigated with Transmission Electron Microscopy (TEM) and Electron Energy-Loss Spectroscopy (EELS). Sample A, a Cr/CrN bi-layer, had a single crystalline structure. Sample B, a CrN single layer with a thickness of more than 1 μm, formed a polycrystalline columnar configuration. High-Resolution TEM (HRTEM) studies revealed that both layers were grown epitaxially on the substrate and the generation of misfit dislocations at the interface has been observed. In both layers edge type dislocations in end-on orientation were found at the CrN/MgO interface and characterized. For a detailed investigation of the strain fields across the interface and around the dislocations cores the Geometric Phase Analysis was applied. Displacement and two-dimensional relative strain maps were calculated. In addition EELS measurements were realized for the CrN single layer. A spatial distribution of the two components (CrN film and MgO substrate) was performed with Multiple Linear Least Squares fitting technique (MLLS fitting).

Kurzfassung

Die Mikrostruktur von zwei CrN Filmen und deren Grenzfläche mit einem MgO-Substrat wurden mit Transmissionselektronenmikroskopie (TEM) und Elektronen-Energieverlust-Spektroskopie (EELS) untersucht. Probe A, eine Cr/CrN-Doppelschicht, hatte eine einkristalline Struktur. Probe B, eine CrN-Einfachschicht mit einer Schichtdicke von mehr als 1 µm, hat einen polykristallinen säulenförmigen Aufbau. Hochauflösende TEM (HRTEM) Untersuchungen ergaben, dass beide Schichten epitaktisch auf dem Substrat aufgewachsen waren. Außerdem wurde in beiden Proben die Bildung von misfit-Versetzungen an der Grenzfläche zwischen MgO und CrN beobachtet. In beiden Fällen handelte es sich um Stufenversetzungen in end-on Orientierung. Für eine detaillierte Untersuchung der Spannungsfelder entlang der Grenzflächen und rund um die Versetzungskerne wurde die geometrische Phasenanalyse eingesetzt. Zwei-dimensionale relative Spannungsverteilungen und Abweichungen von Gitterebenen wurden berechnet. Darüber hinaus wurden EELS Messungen für die CrN-Einfachschicht realisiert. Die Verteilung der beiden Komponenten (CrN-Film und MgO-Substrat) quer zur Grenzfläche wurde mithilfe der Methode der mehrfachen linearen kleinsten Quadrate abgebildet.

Acknowledgements

First and foremost I would like thank Professor Gerhard Dehm for giving me the opportunity to carry out this thesis at the Erich Schmid Institute in Leoben.

Special thanks to Dr. Zaoli Zhang for his everlasting support and patience during the last months.

For their technical support I would like to thank Gabriele Moser for her great help in TEM sample preparation and Dr. Rostislav Daniel for providing all thin films investigated in this thesis. Furthermore I want to thank DI FH Jörg Thomas for many hours of training in TEM techniques.

Thanks to my colleagues for many discussions in all matters, especially to Tristan Harzer for his help with all my problems in the great field of TEM.

I am very grateful to my family and friends for their support through all steps of my life.

Finally, I want to thank Christina Hofer for going with me through all the hard years of study. And very special thanks to my beloved Christian Richter, without him many things would not have been possible.

Contents

1. Introduction

Transition metal nitrides such as titanium nitride and chromium nitride have been one of the hot topics in material science. They are widely used as hard coating materials because of their outstanding properties such as high hardness, mechanical strength, chemical inertness and high temperature stability. This attributes yield to a multiplicity of industrial applications [1]. They are used in the automotive and aerospace sector, in the cutting industry and as optical coatings.

An improvement of the properties of coatings is of great interest to extend the lifetime of tools. Several approaches have been proposed in the scientific community. A great number of nanoscale multilayers have been investigated such as metal/ceramic combinations like Cr/CrN and Ti/TiN or compounds of TiN and CrN [2-5]. The analysis of the surface morphology [6,7], the comparison of different Cr/CrN multilayers in nanoindentation measurements [8] and adhesion tests [2,9] and the microstructural characterization of several single and multilayer coatings have helped improving the coating performance.

An advancement of the layers is always attended by the coating technology. The most common used film deposition processes are the chemical vapor deposition (CVD), the physical vapor deposition (PVD) and the electroplating, in which PVD has an accentuated relevance. To optimize the process parameters and increase film quality a multiplicity of researches has been done. So far, it is known that the substrate temperature has great influence on the microstructure and defect density. Also bias voltage, the quality of the targets and the gas flow are effecting the film growth. For example, the formation of a hexagonal Cr_2N transition layer between Cr and CrN was observed due to changes in the gas flow. It was indicated that a Cr_2N transition layer guarantees good adhesion between Cr and CrN. In summary, it has been shown that bi- or multilayers composed of films with varying properties can have an improved performance compared with single layer films.

A fundamental understanding of the microstructure and chemical composition of the coatings and their interface with the substrate material is essential for the improvement of film quality. The number of defects and their distribution within the layers and across boundaries are affecting especially the mechanical properties. The interface between

film and substrate materials is characterized by a mismatch of the lattices, which leads to the generation of misfit dislocations. Although the defect analysis has been reported in some metal nitride films, there is still a demand for detailed investigations in hard coating nitride films.

Transmission electron microscopy (TEM) is well suited for characterizing the structure and chemistry of materials. With conventional TEM it is possible to make bright-field (BF) and dark-field (DF) images and analyze the defect structure such as dislocation networks with these methods using diffracted or primary beams. High-resolution TEM (HRTEM) reveals the material structure and misfit dislocations with atomic resolution. Therefore the atomic structure and misfit dislocations can be directly visualized. Electron energy-loss spectroscopy (EELS) is besides the X-Ray Energy Dispersive Spectroscopy (XEDS) a very useful technique to determine the composition and chemical bonding. In combination with scanning TEM (STEM) one can reach very high spatial resolution to measure the local chemistry. The outstanding properties of chromium nitride films and the chance to investigate them with highly sophisticated microscopy methods was the motivation to compile this diploma thesis. In particular, the investigation of the interface between the CrN layer and the MgO substrate was of great interest.

For this reason the investigation of two CrN layers has been accomplished to characterize the microstructure and the chemical constitution of the layers and the interface between layer and substrate. From specimen A, a Cr/CrN bi-layer on an MgO substrate, a cross-sectional sample was prepared. From specimen B, a CrN single layer also on an MgO substrate, one cross-sectional and one plan-view sample were made.

One aim of the thesis was to determine the orientation relationship between Cr, CrN and MgO and to analyze misfit dislocations at the CrN/MgO interface. For this task BF, DF and selected area diffraction (SAD) patterns were recorded. Based on HRTEM images and geometric phase analysis (GPA) the distortion of the lattices was investigated. In addition, EELS analysis across the CrN/MgO interface was conducted. Some essential theoretical fundamentals were summarized and the results of all three samples were discussed and compared.

2. Theoretical foundations

TEM is an important tool for material science and is described in several textbooks. Mainly, I want to point out the textbook by Williams and Carter [10], which gives a comprehensive overview of the instrumentation, different imaging techniques such as BF and DF, and also explains advanced microscopy methods like HRTEM, STEM, XEDS and EELS. In addition, I want to mention the Microscopy book of Heimendahl [11], which briefly shows all conventional TEM techniques. A summary of all fundamentals cannot be given here, therefore only the Geometric Phase Analysis (GPA) technique and some basics of EELS will be described below.

2.1. Geometric Phase Analysis

The GPA technique was initially developed by M.J. Hÿtch et al. [12,13]. On the basis of HRTEM images of crystals the distortion of the atomic planes can be used to visualize displacement and strain fields. One can imagine a HRTEM image as a 2D-projection of the atomic crystal structure imaged in certain directions. In a Fourier transform of an image all the periodicities of the crystal are present. In case of a perfect crystal only Bragg reflections (thus sharp spots) would occur, but in case of irregularities in the crystal structure some diffuse intensity will be present around the Bragg spots. Thus, the information of defects such as dislocations in the crystal is present in the Fourier transform (in reciprocal space). Each Fourier component has an amplitude and a phase, which represents the strength and position of the lattice fringes. The intensity $I(\vec{r})$ at a position $\vec{r}$ in the image of a perfect crystal is given by:

$$I(\vec{r}) = \sum_{\boldsymbol{g}} H_g \, exp\,\{2\pi i \vec{g} \cdot \vec{r}\,\} \tag{2.1}$$

where H_g is the Fourier component of the Bragg periodicity $\vec{g}$. The Fourier component H_g has the amplitude A_g and phase P_g and can be defined as followed:

$$H_g(\vec{r}) = A_g(\vec{r})\, exp\{iP_g(\vec{r})\}. \tag{2.2}$$

Variations in the crystal structure can be described now with changes in amplitude and phase of the Bragg spots. The intensity across the image is now given by:

$$I(\vec{r}) = \sum_{\boldsymbol{g}} H_g(\vec{r}) \exp\{2\pi i \vec{g} \cdot \vec{r}\}. \tag{2.3}$$

The phase is connected directly with the displacement field $\vec{u}$:

$$P_g(\vec{r}) = -2\pi \vec{g} \cdot \vec{u} \tag{2.4}$$

A two dimensional displacement field can be defined with two phase images of two non-parallel reflections $\vec{g}_1$ and $\vec{g}_2$:

$$\vec{u} = -\frac{1}{2\pi}\left[P_{g1}(\vec{r})\vec{a}_1 + P_{g2}(\vec{r})\vec{a}_2\right] \tag{2.5}$$

where $\vec{a}_1$ and $\vec{a}_2$ are the vectors for the lattice in real space. Written as a matrix:

$$\begin{pmatrix} u_x \\ u_y \end{pmatrix} = -\frac{1}{2\pi}\begin{pmatrix} a_{1x} & a_{2x} \\ a_{1y} & a_{2y} \end{pmatrix}\begin{pmatrix} P_{g1} \\ P_{g2} \end{pmatrix} \tag{2.6}$$

The gradient of the displacement field *e* and strain field *ε* can now be determined in form of matrices as followed:

$$e = \begin{pmatrix} e_{xx} & e_{xy} \\ e_{yx} & e_{yy} \end{pmatrix} = \begin{pmatrix} \frac{\partial u_x}{\partial x} & \frac{\partial u_x}{\partial y} \\ \frac{\partial u_y}{\partial x} & \frac{\partial u_y}{\partial y} \end{pmatrix} \tag{2.7}$$

$$\varepsilon = \frac{1}{2}(e + e^T) = \begin{pmatrix} \varepsilon_{xx} & \varepsilon_{xy} \\ \varepsilon_{xy} & \varepsilon_{yy} \end{pmatrix} \tag{2.8}$$

where T denotes the transpose of the matrix. This procedure has been implemented in the Digital Micrograph software and the practical application will be shortly described below step by step.

1. A HRTEM image is required for the analysis.
2. First a so-called power spectrum is calculated, which is a modular squared fast Fourier transform (FFT) of the image.
3. Then two spots of non-parallel reflections in the FFT are selected with masks, in our case cosine masks with a radius of ¼$\vec{g}$.
4. Now the phase images are calculated. They show which periodicities are present in the HRTEM image.
5. A reference region which represents the perfect crystal is chosen in one phase image with a region of interest (ROI) box.
6. Finally with two phase images a two-dimensional strain map can be computed. The rotation and fringe deformation can be also visualized in this way.

2.2. EELS in the TEM

EELS is based on the inelastic scattering of electrons in the specimen. When primary electrons travel through the specimen, they may ionize an atom by exciting an inner core-shell electron into empty states above the Fermi energy level. The primary electrons loose energy and the atom emits characteristic irradiation (for example X-Ray or Auger electrons) by getting back in the ground state. The energy loss of the incident electrons depends on the sample material and can be used therefore for elemental characterization. But EELS offers more than just elemental identification. It also provides information about the electronic structure, the sample thickness of the specimen, etc..

The energy-loss spectrum can be divided in three parts, the zero loss, the low-loss and the high-loss (or core-loss) region. At the beginning of the spectrum the zero-loss peak (ZLP) appears (see Fig. 2.1a), which is very intense and contains all unscattered and elastically scattered electrons. The low-loss region ranges from the ZLP up to 50 eV and contains the plasmon peak and information from the more weakly bound electrons in the material. At higher energy-loss the intensity is decreasing strongly. In the high-loss region as seen in Fig 2.1b characteristic ionization edges appear above the background. They contain information about more tightly bond core-shell electrons and thus information about the bonding mechanism and the atomic distribution. Some important experimental details are described below.

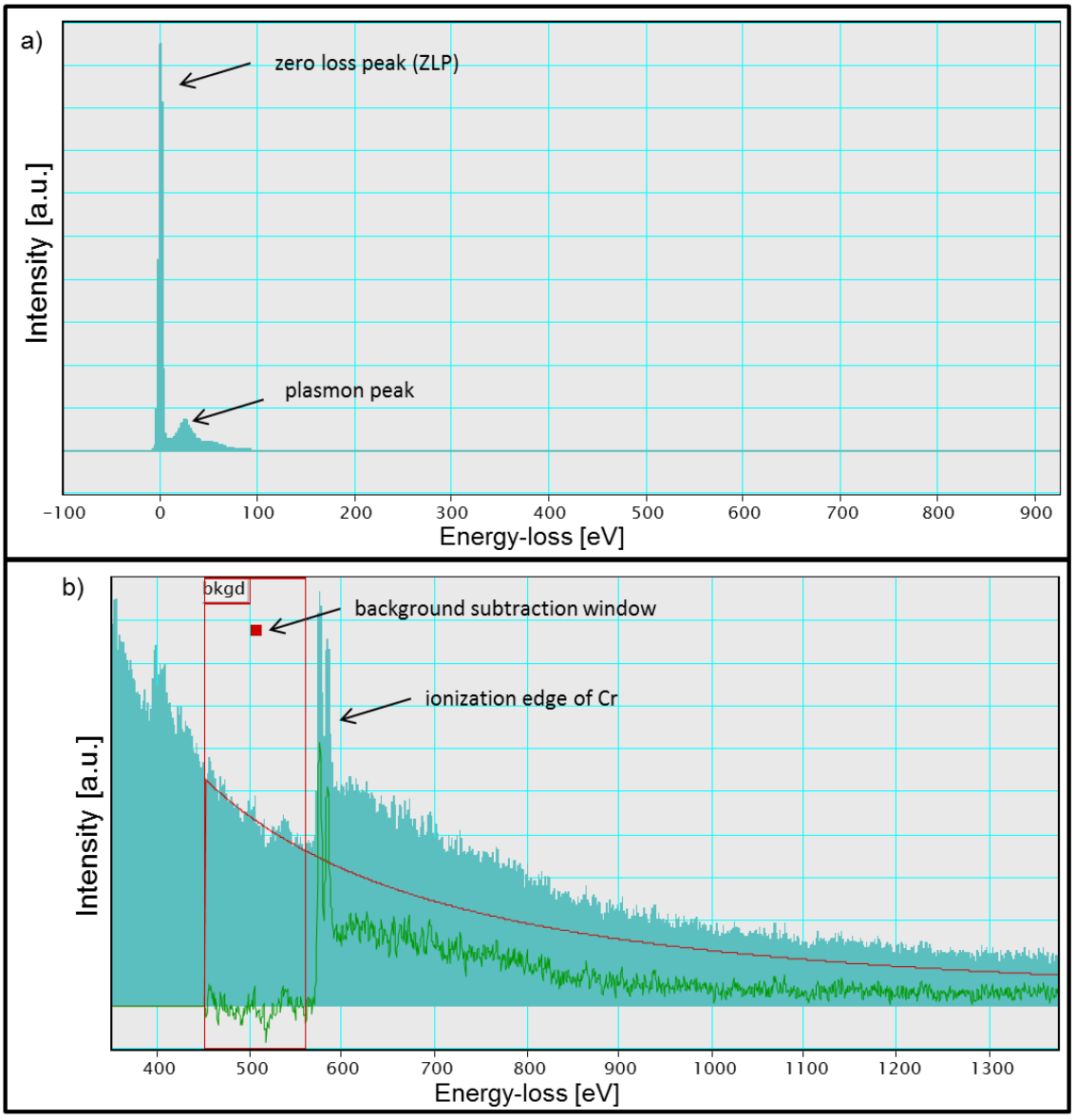

Figure 2.1: a) Low-loss spectrum of CrN; b) core-loss spectrum of CrN.

The EELS instrumentation can be realized in a conventional TEM with a magnetic-prism beneath the viewing chamber, a so-called post-column filter, or with a TEM containing an in-column imaging filter. The EELS experiments can be also performed in a STEM mode. In the STEM mode a very small probe is formed with strong electromagnetic lenses. The probe is scanned across the specimen. With annular detectors one can record DF images from strongly scattered electrons and form simultaneously an EEL spectrum with electrons scattered at smaller angles. This collection angle is determined by an energy-selecting slit also called entrance aperture d_e, because it marks the entrance of the spectrometer. In Fig. 2.2a schematic drawing of the electron path

through the specimen into the spectrometer is shown. Two semi-angles are important to optimize the experimental settings: the convergence semi-angle α and the collection semi-angle β. The convergence semi-angle depends on the microscope´s adjustment, mainly the condenser lens and aperture. The collection semi-angle is determined by the objective aperture, the spectrometer entrance aperture, the camera length and the mechanical specification of the instrument.

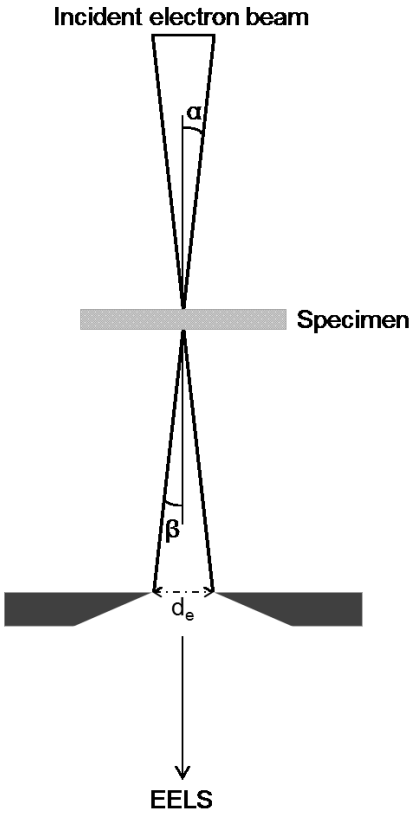

Figure 2.2: Schematic diagram of electron path through the specimen into the EELS system; α…convergence semi-angle; β…collection semi-angle; d_e…entrance aperture size.

As mentioned before a background is present in the spectrum. The background and the core-loss edges are dependent on the collection semi-angle. Both signals are getting stronger with increasing angle, but the background signal under the edge is increasing faster. The signal-to-background ratio, also called jump ratio is the highest at small collection semi-angles. But the angle should be also large enough to collect a significant part of the scattered electrons. As a rule of thumb the collection semi-angle should be three times the characteristic scattering angle for the edge energy [14]. The determination of the collection semi-angle is therefore of great interest. For a quantitative analysis an integration over the intensity of the ionization edge has to be

done. But the background has to be removed before. It is also necessary to know the number of atoms which generate the intensity. Therefore, the partial ionization cross section

has to be determined. Different background subtraction methods and ionization

models are described in a textbook about EELS by Egerton [15].The most important points are described here:

1. The sample region has to be very thin to reduce plural scattering, which causes the background signal.
2. The energy-loss range has to be chosen considering which elemental signals have to be in the spectrum. The range is defined by the start energy and the energy dispersion and the number of channels provided by the Charge-coupled device (CCD). In our case a dispersion of 0.5 eV/channel and 2000 channels lead to an energy-loss range window of 1000 eV.
3. The acquisition time has to be chosen carefully to avoid saturation of the CCD.
4. The background has to be subtracted with an appropriate method. Therefore, an energy-loss range of at least 40 eV is needed in front of the edge (see red background subtraction window in Fig. 2.1b). The signal window has also to be large enough to catch the whole ionization edge.
5. The ionization cross section has to be determined with an adequate model.
6. In case of peak overlapping advanced fitting and quantification techniques such as the multiple linear least squares fitting technique (MLLS) has to be applied.

As mentioned before EELS can provide more information than only elemental identification from the core-loss edges. It is also possible to determine the specimen thickness from the ZLP and the low-loss region. The energy-loss near edge structure (ELNES) gives information about the valence state, bonding and atom coordinates and can be used as `fingerprints´, such as shown in the literature [16]. The extended energy-

loss fine structure (EXELFS) gives information about the atom-specific radial distribution of nearest neighbors. In the low-loss region the plasmon peak offers information about valence or conduction electron density. The core-loss edges define the elemental composition. In sum EELS is a very powerful experimental technique, which provides much more information compared with XEDS technique.

3. Literature review

Some publications relevant to this thesis are summarized below.

H. Era et al. [17] investigated the influence of the nitrogen pressure on CrN films during the deposition process. They used stainless steel as substrates, and the films were deposited by reactive sputtering. The coatings were analyzed by Transmission electron microscopy (TEM) and X-ray diffraction (XRD) to determine crystal structure and nitrogen content. They demonstrated that with increasing N_2 pressure (p_{N2}) the nitrogen content increases and the chromium content decreases. This leads to a change in the crystal structure from the hexagonal Cr_2N at lower pressure to cubic CrN. At intermediate nitrogen content the coating was a mixture of Cr_2N and CrN. The cross-section TEM images show a dendritic structure for the hexagonal closest packed Cr_2N, while CrN grows in a columnar structure. The lattice constants of the chromium nitrides were also changing with the nitrogen pressure. The lattice constant of CrN is increasing with increasing nitrogen content. The a-axis of Cr_2N is elongating with increasing nitrogen content, the c-axis is decreasing.

J. Romero et al. [8] analyzed multilayer systems, so-called superlattices, consisting of a metal and a ceramic compound. They deposited films by reactive sputtering with alternating pure chromium and chromium nitride layers on silicon substrates. The total thickness of the layers was about 1 µm with bilayer periods ranging between 2 nm to 120 nm. High-angle XRD patterns showed a modification of the preferred orientations with changing bilayer period (Λ). At large periods the (200) orientation is favored for Cr and for CrN. For CrN in the thickest (period of 120 nm) and thinnest bilayers (Λ < 4 nm) the (111) peak appears, for the thickest also the (311) reflection is present. Due to a potential stress evolution the position of the CrN (200) peak shifts to higher tensile values with decreasing layer thickness until Λ = 6nm. The peak is also getting broader and the positions changes abrupt to compressive values for thinner layers (< 5 nm). This behaviour is also observed for the CrN (400) peak. The reflections of the chromium layers are also changing for different bilayer periods. The Cr (200) peak is broadening and the intensity is decreasing with decreasing bilayer period, but no shift of the peak position was observed. At a bilayer period of about 5 nm the Cr (200) reflection disappears and the (211) orientation is now favored. On the basis of TEM micrographs and SAD patterns the crystallographic orientation was determined. A single crystalline

region of a multilayer with a bilayer period of 120 nm was analysed. The diffraction pattern (DP) showed that the Cr is oriented in [100] zone axis and the CrN layer in [110] zone axis. The orientation relationship is therefore given by Cr (001) II CrN (100) and Cr [100] II CrN [110]. The (100) growth direction of the Cr layer is rotated around 45° with respect to the growth axis of the CrN, which leads to a very low mismatch (1.6 %). In addition the mechanical properties were analyzed by nanoindentation. The multilayer reached hardness values about 30 GPa in the nanometric range, which is two times higher than expected from the rule-of-mixtures.

S. Han et al. [18] investigated the influence of an electroplated Cr interlayer on the microstructure of CrN films on steel substrates. They compared two samples, one with and one without an interlayer (CrN/steel and CrN/Cr/steel). The characterization was performed with XRD, cross-sectional TEM and SAD. Both samples showed columnar structure, for the CrN/steel coating the columnar structure was less evident, strong and upward compared with CrN/Cr/steel coating. The XRD measurements showed that the preferred orientation for the CrN/Cr/steel coating is the (220). The TEM investigations the thickness of both CrN layers was 1.2 µm. The diffraction pattern revealed a strong texturing for the CrN layer on the Cr film. Instead of continuous rings only short CrN{220} and {200} arcs were observed. Also the Cr layer is textured, the growth direction was determined as Cr{200}. TEM micrographs showed that a transition interlayer of about 225 nm thickness was formed between the Cr and the CrN layer. The phase of the interlayer was not fully identified. Other studies suggest a possible formation of CrN_x and Cr_2N phases. Also for the CrN/steel coating the formation of an interlayer (6 nm thick) was observed. HRTEM analysis exhibits that the interlayer between CrN and Cr is crystalline. The interlayer between CrN and steel has a small amount of amorphous phases, also the interlayer of between Cr and steel. In the Cr layer voids have been noticed, possibly due to hydrogen formation at the beginning of the electroplating process.

The Cr(001) layers analyzed by C.-M. Wang et al. [19] were deposited by molecular beam epitaxy on MgO (100) substrates. The films were grown at room temperature and at 550 °C and had a thickness of about 100 nm. The coatings were analyzed by HRTEM, SAD patterns and EELS. It was shown that the film grown at room temperature has a highly oriented columnar structure while the film grown at 550 °C was single crystalline. The Cr(001) single crystal was grown rotated about 45° with respect to the substrate. Based on the basis of SAD patterns the orientation relationship was determined as the following: MgO [100]IICr [110] and MgO (001)IICr (001). Due to this

rotated epitaxial growth, the mismatch between Cr and MgO is minimized and the expected misfit dislocation spacing is about 6.25 nm. The HRTEM images showed that misfit dislocations are created at the interface by inserting extra (110)-planes on the Cr side. The observed distance between the dislocations was 4.64 nm for the film grown at 550 °C and 5.38 nm for the film grown at room temperature. A Burgers circuit was drawn to define the Burgers vector $\mathbf{b}=a_{Cr}[110]$. The EELS results indicated that there is no chemical intermixing of Cr and MgO within the range of 1.5 nm from the interface.

S. Cazottes et al. [20] characterized the interface between Cu and MgO with HRTEM imaging. The misfit is about 14 %. Two copper films were deposited on MgO(001) by magnetron sputtering. For the analysis in <100> viewing direction a 2 µm thick film was grown, for the <110> observation the film was 1.2 µm thick. They were deposited under different process parameters. For HRTEM imaging two cross-sectional samples were prepared. In the <100> viewing direction they observed misfit dislocations approximately every seventh (020)-planes using C_S-corrected HRTEM imaging. To restore the continuity of the (020) planes across the interface the Cu planes were bent at the dislocation cores. The interface showed surface steps on the MgO substrate. By drawing Burgers circuits the Burgers vector was determined as $\mathbf{b}=½a_{Cu}<100>$, therefore it is a <100> dislocation network. The distance between the misfit dislocations was 1.37±0.05 nm, which is 7% higher than the theoretical value of 1.28 nm. Therefore the misfit strain is not fully compensated by misfit dislocations. Based on GPA the displacement of the (020) d-spacing was mapped to characterize the dislocations and the interface. In the <110> imaging direction they observed also misfit dislocations and a rotation of the Cu layer of around 3% relative to the MgO substrate. The projected Burgers vector was determined as $\mathbf{b}=½a_{Cu}<110>$. The dislocation distance was 0.93±0.08 nm, which suggests that a <100> dislocation network is present as in the first sample.

P. Wiecinski et al. [2] characterized different (Cr/CrN)x8 multilayer systems on titanium alloy substrates deposited by plasma assisted physical vapor deposition (PAPVD). Cross-sectional samples have been prepared by focused ion beam milling and analyzed with scanning electron microscopy (SEM) with XEDS and C_S-corrected STEM. The coatings had a total thickness of 5-6 µm with varying thickness ratio of Cr and CrN layers. The STEM images showed that the layers are nanocrystalline and of homogenous thickness. In the STEM dark field operated in Z-contrast mode the Cr layers appear brighter than the CrN layers due to stronger beam scattering. Phases with higher atomic weight are thus brighter. These results were confirmed by XEDS spectral imaging. The microstructure was characterized by TEM micrographs and diffraction

patterns. Both layers were grown in a columnar structure. They observed besides the bcc Cr and the fcc CrN a Cr_2N interlayer formed between the Cr and the CrN during the deposition process because of varying nitrogen flows. They also performed hardness measurements and investigated the adhesion behavior of the multilayers using scratch tests. The hardness values were increasing with decreasing Cr/CrN ratio, possibly because the volume fracture of the harder CrN phase is getting higher. Between the highest and the lowest measured hardness value was a difference of 25%. A similar but weaker trend was observed in Young`s modulus changes. The scratch tests showed that at loads of 25-70 N the adhesive failures started and at higher loads a total delamination of the coating occurs. The soft Cr layer improved the tribological behavior, the best adhesion was observed at a Cr/CrN ratio close to 0.5.

C. Mitterbauer et al. [16] performed detailed EELS measurements on CrN and Cr_2N powder samples. The chromium nitrides have different crystallographic structure; therefore they also have a different ELNES. This enables the scientists to collect so-called ´fingerprints` and with it the identification of common features in the ELNES. In the low loss region CrN shows compared to Cr_2N a minimum in the range of 13 – 17 eV before the main peak appears at 26 eV; the Cr $M_{2,3}$ edge (at 42 eV) of Cr_2N is broad while the CrN edge is structured. In the core-loss region the two compounds have different ELNES of the N-K edge (at about 400 eV). The N-K edge of CrN is divided into two peaks and shows overall four features between 399.0 and 410.8 eV. In contrast Cr_2N exhibits only one main peak and a broad shoulder behind. The spectrum of Cr_2N shows in addition an O-K edge at about 530 eV due to the contamination. The L_3/L_2 ratio of the Cr-$L_{2,3}$ edges is varying for CrN and Cr_2N. Based on all these differences in the ELNES one can distinguish between cubic CrN and hcp Cr_2N.

C. Mitterbauer et al. [21] also observed the changes in the ELNES of chromium nitride films (CrN and $Cr_{0.47}N_{0.53}$) introduced by electron irradiation in the TEM. The layers were deposited by reactive magnetron sputtering on silicon wafers. They collected EEL spectra every 30 s, the last at 300 s at a maximum current density of ~ $2x10^6$ A/m^2. For comparison they used a spectrum of a CrN powder sample with a purity of > 99% as reference. The powder sample shows no sensitivity to the electron irradiation, while the CrN film samples show in addition to the N-K edge at 399.0 eV the appearance of a second peak at 401.1 eV when increasing the electron dose. This peak is more pronounced in the $Cr_{0.47}N_{0.53}$ film, while the stoichiometric CrN film remains nearly unaffected. The peak at 401.4 eV could appear because of a 1s-π*-transition of molecular nitrogen located in interstitial positions.

4. Experimental procedure

4.1. Film deposition

The two coatings (sample A and B) investigated in this thesis were grown on MgO substrates with the size of 10 mm x 10 mm x 1 mm using unbalanced magnetron sputter deposition. A hot isostatic pressed chromium target with a diameter of 145 mm was used. Sample A is a Cr/CrN bi-layer with a total thickness of about 20 nm (required from the deposition process). The sputtering process of the CrN film was carried out in an Argon-Nitrogen-mixture with a N_2 partial pressure of 0.5 Pa and a total pressure of 1 Pa. The bias voltage was – 80 V. The Cr film was deposited in a pure Argon atmosphere with a total pressure of 1 Pa and a bias voltage of – 40 V. The substrate temperature during the sputtering process was 500 °C; the sputtering power was 2 kW. Sample B is a CrN single layer (over 1 µm thick) and was produced in Argon - N_2 gas mixture where the N_2 partial pressure was 0.25 Pa and the total pressure was 1 Pa. The bias voltage was – 40 V and the sputtering power was 6 kW at a substrate temperature of 350 °C.

4.2. TEM sample preparation

4.2.1. Cross-sectional sample preparation

The cross-sectional samples were prepared with a method developed by Strecker et al. [22], the procedure is shown in Fig. 4.1. The bulk material was cut into 2 mm stripes with a diamond wire saw and glued face to face with EpoxyBond110 on the sides with the layers. This so-called sandwich was ground down to 600 µm and glued into a ceramic tube. The tube was sliced into circular disks, which were ground down to 100 µm and polished. Afterwards the disks were dimple grinded and polished, so that the thickness in the center of the disk was about 10 µm. Finally the sample was ion milled till perforation with a precision ion polishing system (Model 691) of Gatan. The CrN single layer was ion milled for about 2 hours at a temperature of – 40 °C with an

acceleration voltage of 4 kV and at an incidence angle of 6°. The Cr/CrN bi-layer was ion milled for about 4 hours. A thin film of amorphous carbon was deposited to avoid charging of the sample.

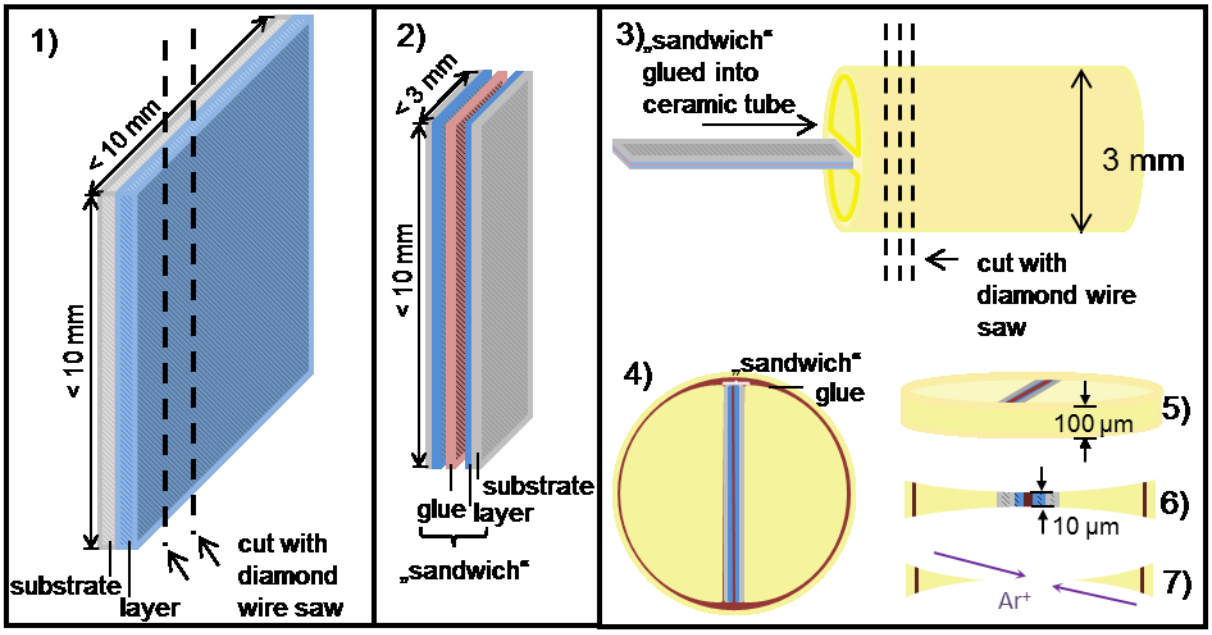

Figure 4.1: Schematic drawing of the cross-sectional sample preparation route; 1) bulk material cut into stripes with a diamond wire saw; 2) „sandwich" with two material stripes glued face to face on the film side; 3) "sandwich" glued into ceramic tube and cut into circular disks; 4) top view on the disk; 5) disk ground down to 100µm and polished; 6) disk dimple ground down to 10 µm in the center and polished; 7) ion milling till perforation.

4.2.2. Plan-view sample preparation

For the preparation of a plan-view sample a circular disk was cut out of the bulk material using an ultrasonic disk cutter (Gatan model 601 with boron nitride). Then the disk was ground on the substrate side until a thickness of 100 µm was reached, followed by dimple grinding and polishing until the center had a thickness of 10 µm. Afterwards the sample was ion milled from the substrate side till perforation. The preparation route is shown schematically in Fig. 4.2.

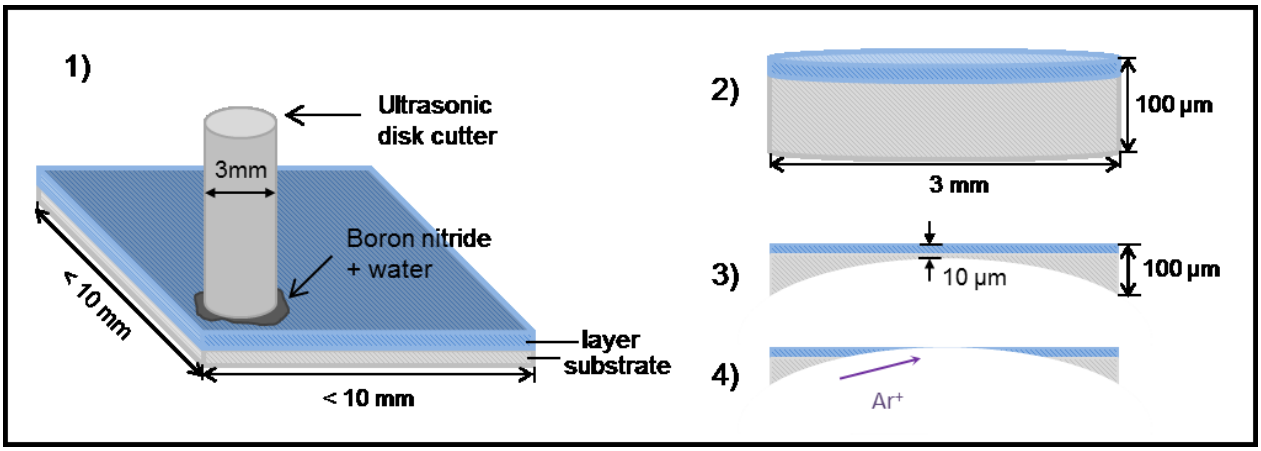

Figure 4.2: Schematic drawing of the plan-view sample preparation route; 1) bulk material: disks cut out with a diameter of 3 mm; 2) disk ground down to 100 µm; 3) disk dimple ground down to 10 µm and polished; 4) ion milled till perforation from the substrate side.

4.3. Microscopes

The micrographs in this thesis were recorded on the Transmission Electron Microscopes TEM CM12 (Philips) and on the JEM 2100F (Jeol) at the Erich Schmid Institute of Materials Science in Leoben, which is a research institute of the Austrian Academy of Sciences.

The CM12 was operated with an acceleration voltage of 120 kV and a LaB_6-cathode. The micrographs were recorded with a 1024 x 1024 CCD-camera MSC BioScan (Model 794 of Gatan).

HRTEM and STEM images and the EEL spectra were recorded with the JEM 2100F microscope. This TEM is equipped with a C_S-corrector (CEOS) and a field emission gun operated at 200 kV. The micrographs were recorded with a 2k x 4k Gatan Orius camera.

Image processing and GPA was performed with the Gatan Digital Micrograph program (version 1.84.1282).

4.4. EELS measurements

The EEL spectra were recorded on a Jeol 2100F equipped with a Gatan imaging filter (Tridiem). The microscope was operated in STEM mode (200kV) with a probe size of 0.2 nm. The measurements were made with a collection semi-angle of 7.5 mrad and a convergence semi-angle of 10 mrad. A spectrometer dispersion of 0.5 eV/channel was used. The spectra were recorded from very thin specimen regions ($t/\lambda < 0.6$; with specimen thickness t and inelastic mean free path λ) with a probe current of 37 pA/cm^2. The acquisition time for the core-loss spectra was 1 s, for the low-loss spectra 0.1 ms. The EELS data processing was performed with MLLS fitting. For the background subtraction the power law model was applied and the Hartree-Slater model for the calculations of the cross-sections.

5. Results

5.1. Sample A: Cr/CrN bi-layer on MgO

5.1.1. Conventional TEM

Sample A consists of two layers, one CrN film grown on the MgO substrate and a Cr film as the top layer. An overview of the layer system is shown in Fig. 5.1a. Both films have a homogeneous thickness. No grain boundaries, cracks or pores have been observed.

The BF image in Fig. 5.1b and the weak-beam DF (WBDF) image in Fig. 5.1c were recorded in a two beam condition ($\vec{g}/3\vec{g}$) using $\vec{g}_{200}$ (see inset). One can differ between the two layers due to their different contrast. The top layer is the Cr layer which shows a brighter contrast than the CrN film sandwiched between the Cr and the MgO substrate. In the WBDF image the contrast is inverted, very dark regions appear bright now. The CrN layer shows more contrast variations. The CrN layer is approximately 10 nm thick, the Cr-layer around 18 nm.

To determine the orientation the MgO substrate was tilted in [011] zone axis. As indicated in the diffraction pattern in Fig. 5.1d the CrN layer is also in [011] zone axis, while the pure chromium layer is oriented in the [001] direction. The pattern was recorded with a SAD aperture (40 µm). The stronger spots (indexed in black color) belong to the CrN and the MgO substrate, because of the small mismatch it is not possible to distinguish between the two of them; the weaker spots (indexed in grey color) belong to the Cr film. The epitaxial relationship between the bcc-Cr and the fcc-CrN is the following: Cr (100) ∥ CrN (100) and Cr [001] ∥ CrN [011]. In Fig 5.1f the MgO substrate was tilted to [001] zone axis, hence the CrN layer is also oriented in [001], while the pure Cr film is in [011] orientation. The SAD pattern reveals that both layers are grown single crystalline.

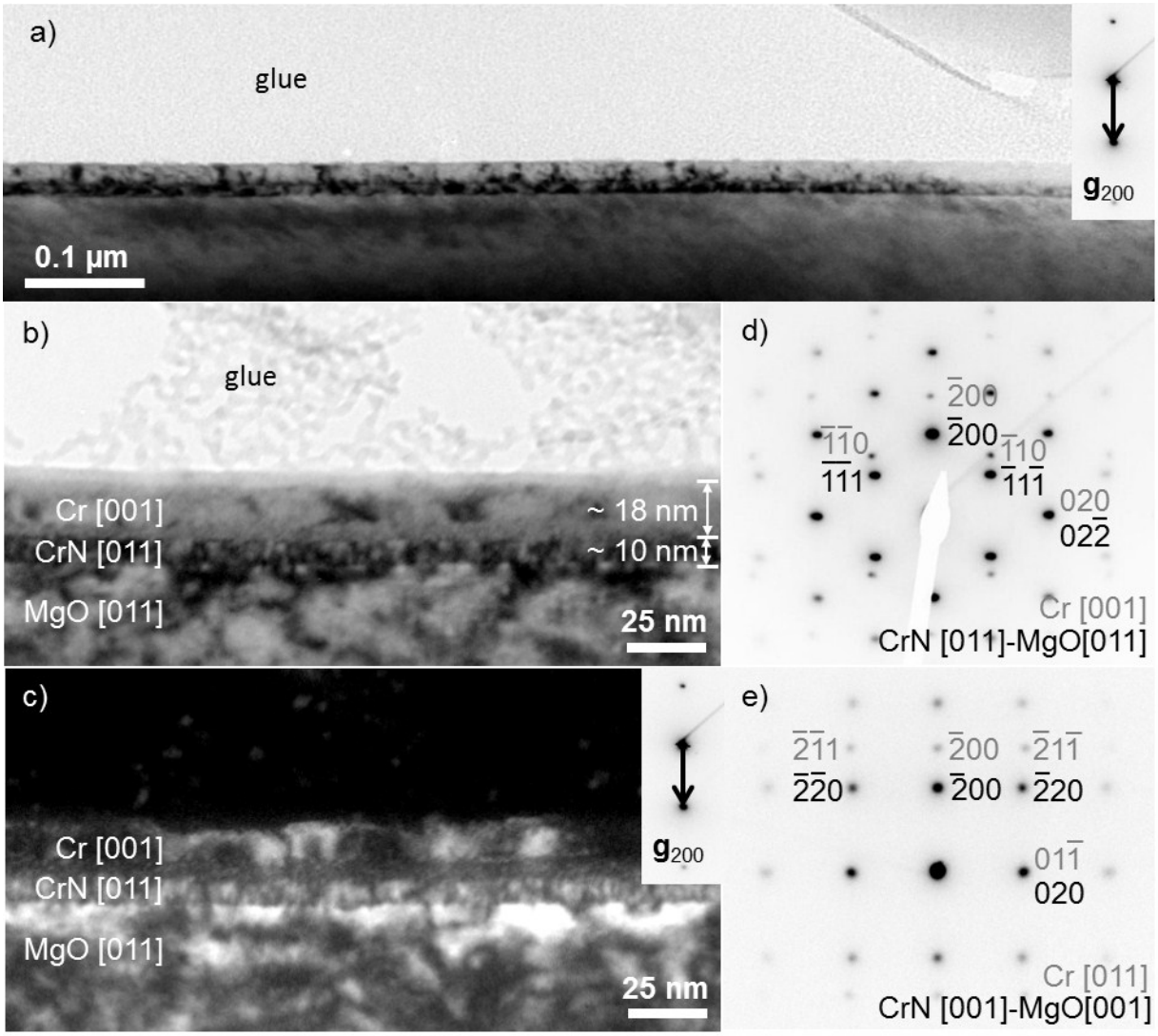

Figure 5.1: Conventional TEM images: a) overview image of the bi-layer; b) detailed BF image; c) detailed WBDF image; d) SAD in [011] zone axis of CrN/MgO; e) SAD in [001] zone axis for CrN/MgO; the contrast in d) and e) is inverted.

5.1.2. ADF-STEM

An ADF-STEM image of the sample is shown in Fig. 5.2. A line profile was drawn across the interfaces and the intensity changes were used to make an accurate determination of the layer thickness. The line profile was averaged over a width of ~60 nm. One can see that an amorphous layer has formed on the surface (the amorphous character of the layer was verified by HRTEM studies). The layer thickness of Cr is about 13.5 nm, which is smaller than measured on the basis of contrast changes in the conventional TEM image.

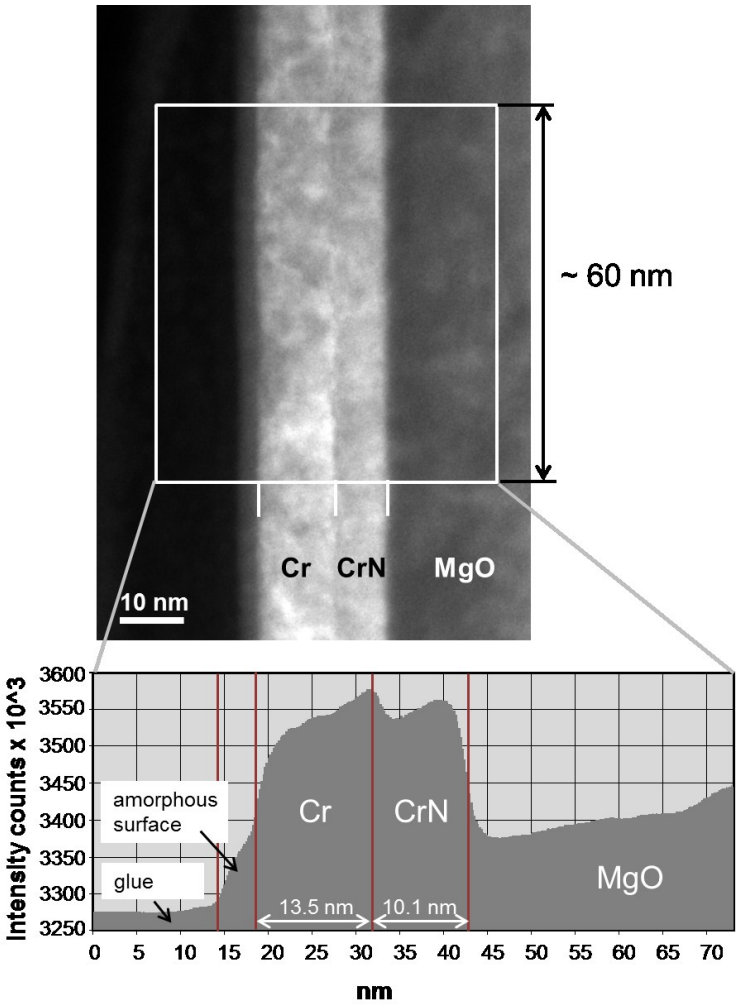

Figure 5.2: ADF-STEM image of the Cr/CrN bi-layer on MgO with intensity evolution across the both layers averaged over a width of ~60 nm.

5.1.3. HRTEM and GPA

A detailed characterization of the interface between the CrN layer and the MgO substrate was realized with HRTEM imaging and GPA. Therefore thin specimen regions were chosen and the MgO substrate tilted in [011] zone axis. A HRTEM image of the Cr/CrN bi-layer is shown in Fig. 5.3a. From the atomic structure it is visible that the CrN layer has the same orientation as the substrate. The interface CrN/MgO appears not atomically abrupt. The Cr layer in [001] orientation is blurred and shows contrast variations at the interface region indicating a diffuse interface between Cr and CrN. The result of the atomic displacement map calculated with the GPA is shown in Fig. 5.3b. The selected reflections are marked in the power spectrum of Fig. 5.3c (it is the $(0\bar{2}2)$ for CrN/MgO and the $(0\bar{2}0)$ for Cr). The deviations of the lattice plane spacings were calculated in the corresponding directions. The MgO substrate was chosen as reference lattice, indicated by the area marked with a red rectangle in Fig. 5.3a. This region represents the undistorted lattice. One can see some small regions of larger displacements at the interfaces as well as in the layers. Changes in the lattice spacings lead to strong variations in the color contrast. Regions in the red color range reveal relatively compressed areas, the distance between lattice planes is thus smaller than in the reference; while blue and pink means relative expansion. The interfaces are not perfectly flat and in particular the layers show a lot of irregularities in the displacement map due to defects. In table 5.1 mean values and standard deviations for three regions are listed (see marked areas in Fig. 5.3b). The distortion of the $(02\bar{2})$ lattice planes in the MgO substrate is nearly zero, while the CrN and the Cr film are due to their smaller lattice constants relatively compressed compared to the $(02\bar{2})$ lattice plane spacing of the substrate. The CrN$(02\bar{2})$ lattice planes are compressed by 1.73% relative to the substrate, the Cr $(0\bar{2}0)$ lattice planes by 3.24%.

To relax the strain misfit dislocations are generated at the interface. In the HRTEM image of the interface between the CrN layer and the MgO substrate in Fig. 5.4a three dislocations are marked with arrows. Two of them are positioned at the interface, and one is inside the CrN layer. The distance between the misfit dislocations is about 7.5 nm. In the [011] projection it can be difficult to see the dislocations, for a better view the image is tilted in Fig. 5.4b. Now it is easier to identify the inserted planes and thus the positions of the dislocations (marked with arrows).

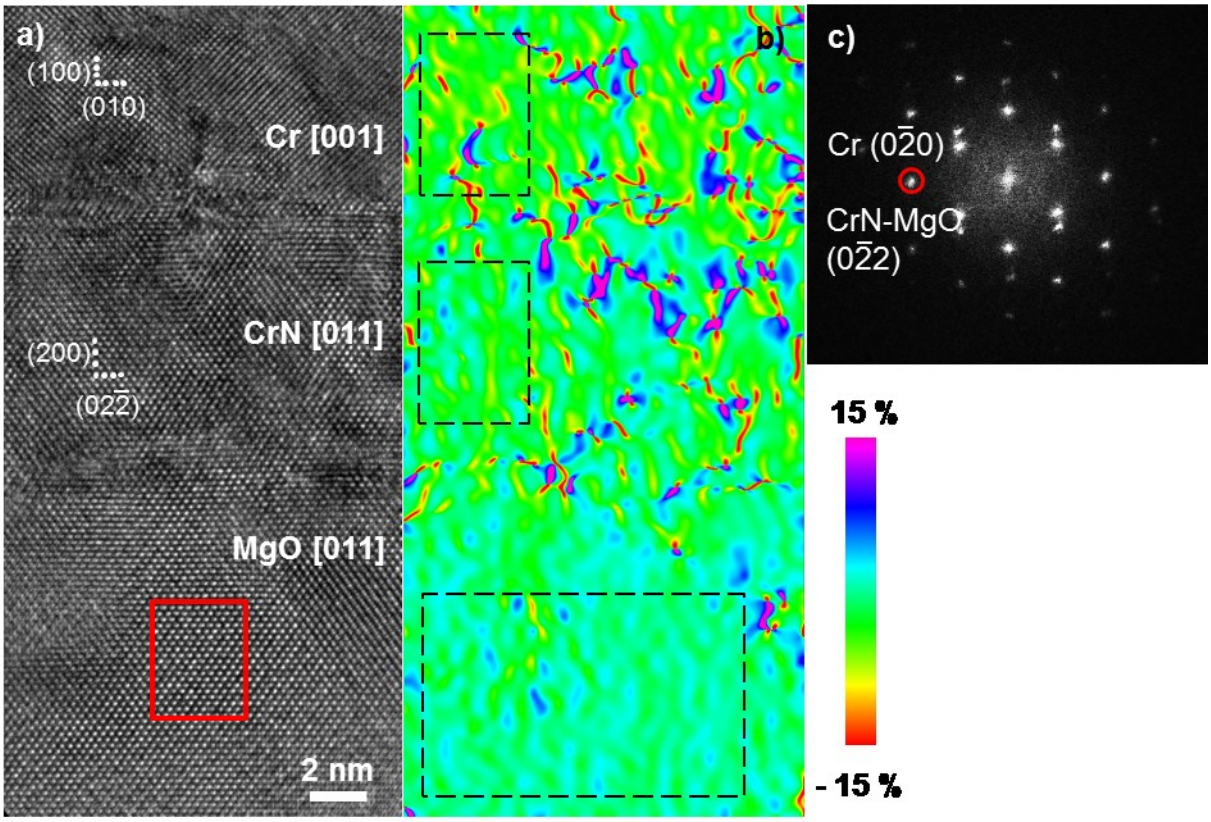

Figure 5.3: a) HRTEM image of the bi-layer; b) GPA of the HRTEM image; c) power spectrum of a) with the selected reflections marked by a red circle.

Table 5.1: Displacement values of the MgO substrate compared to the Cr and the CrN films. Positive values indicate a lattice expansion, negative values a lattice contraction.

Displacement	Mean values [%]	Standard deviation [%]
MgO	- 0.08	1.5
CrN	- 1.73	2.2
Cr	- 3.52	4.5

For an exact determination of the additional planes Bragg filtered images were made (see Fig. 5.4c, d, e and f). Therefore, masks were applied around the spots $\pm\vec{g}$ in the Fourier transform of the image (used reflections are encircled). By taking the inverse Fourier transform the crystal planes according to the selected $\vec{g}$ spots get visible. The extra planes are also drawn in the high resolution image (Fig. 5.4c). In 5.4d one additional (111) plane is visible, in Fig. 5.4e one (200) plane parallel to the MgO surface is inserted. Fig. 5.4f reveals two additional (111) planes.

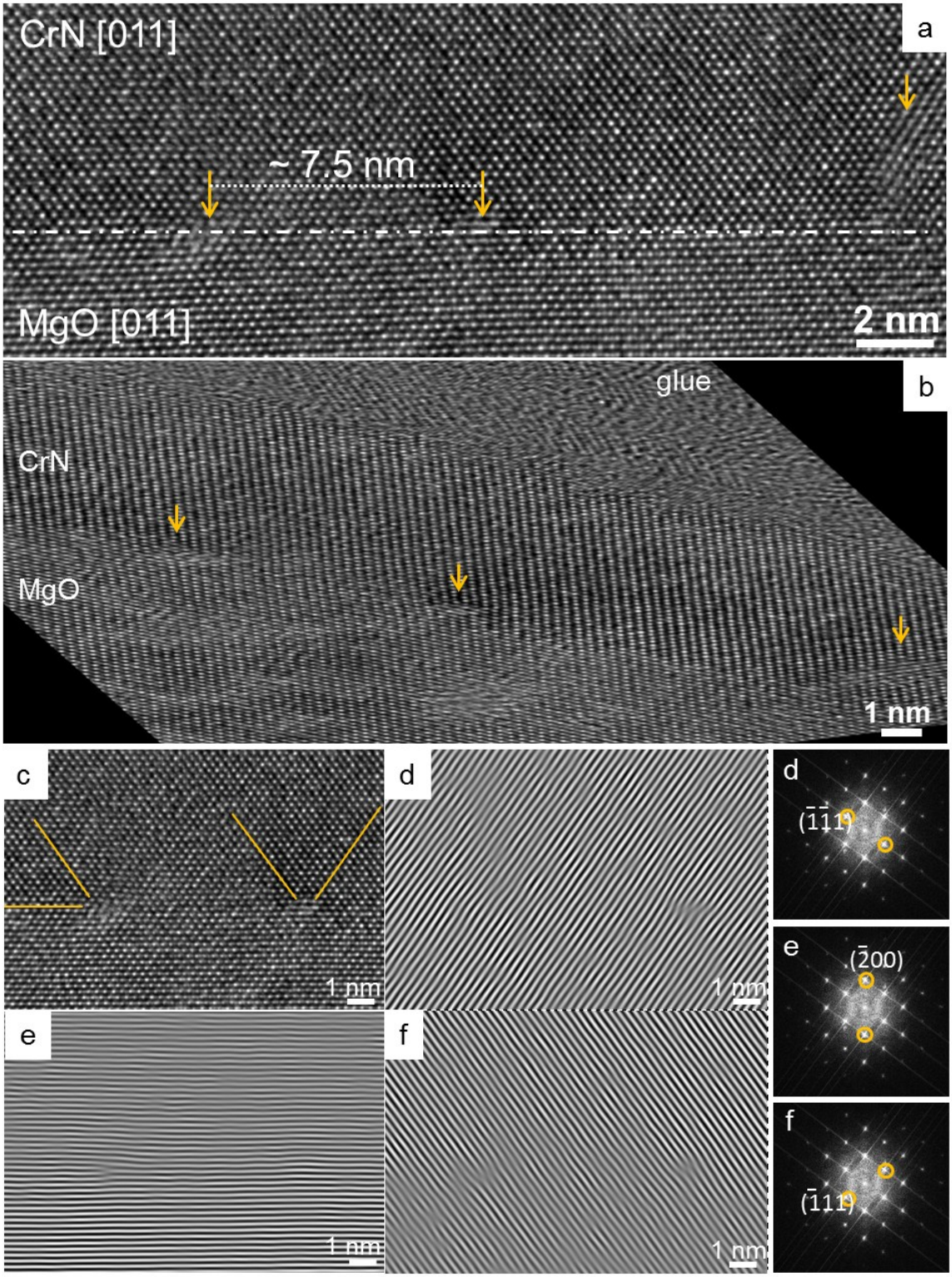

Figure 5.4: a) HRTEM image of the CrN/MgO interface; b) tilted view (Scheimpflug projection); c) detail with two dislocations; d), e), f) Bragg-filtered images with the corresponding selected reflections.

In Fig. 5.5 the Burgers circuits with associated Burgers vectors (red arrows) were drawn to analyze the type of the dislocations. The white dots are indicating the atom column positions. The closure failure represents the Burgers vector. The Burgers vector of dislocation 1 (Fig. 5.5b) is not parallel to the interface; therefore it has a mixed character. The edge component of the dislocation is $|\vec{b}|$= ¼a_{CrN}<110>. The dislocation 2 (Fig. 5.5c) is a pure edge dislocation with a projected Burgers vector of $|\vec{b}|$= ½a_{CrN}<110>. The contrast around the dislocation cores is diffuse.

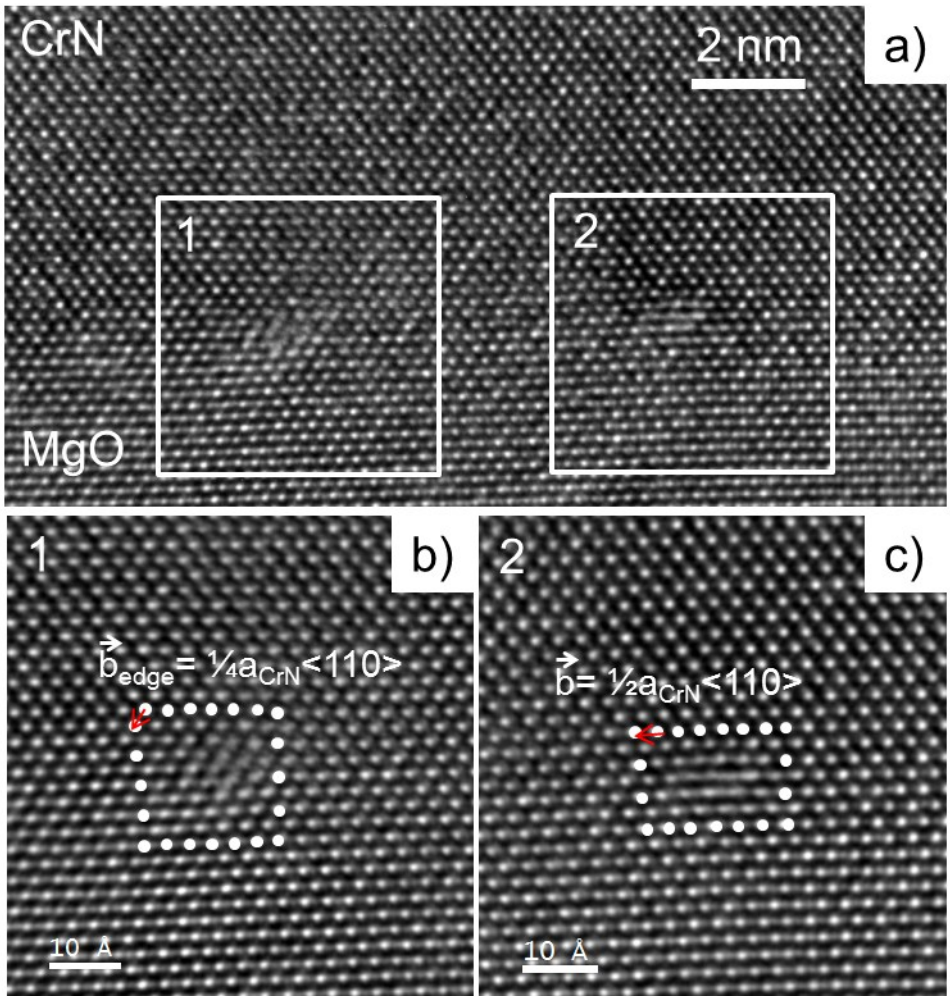

Figure 5.5: a) HRTEM image of CrN/MgO interface; b) Wiener filtered detailed image of dislocation 1; c) Wiener-filtered detailed image of dislocation 2.

For a detailed characterization GPA was applied. The method is very useful to visualize the strain and displacement fields around the dislocation cores. First the phase images

for the $(1\bar{1}1)$ and the $(\bar{2}00)$ reflections were calculated (see Fig. 5.6c and d). Again the MgO substrate was chosen as reference (red and yellow rectangle). Therefore, the phase in the substrate is zero. At the dislocation cores a discontinuity and phase shifts appear; the color changes from black (-π) to white (+π).

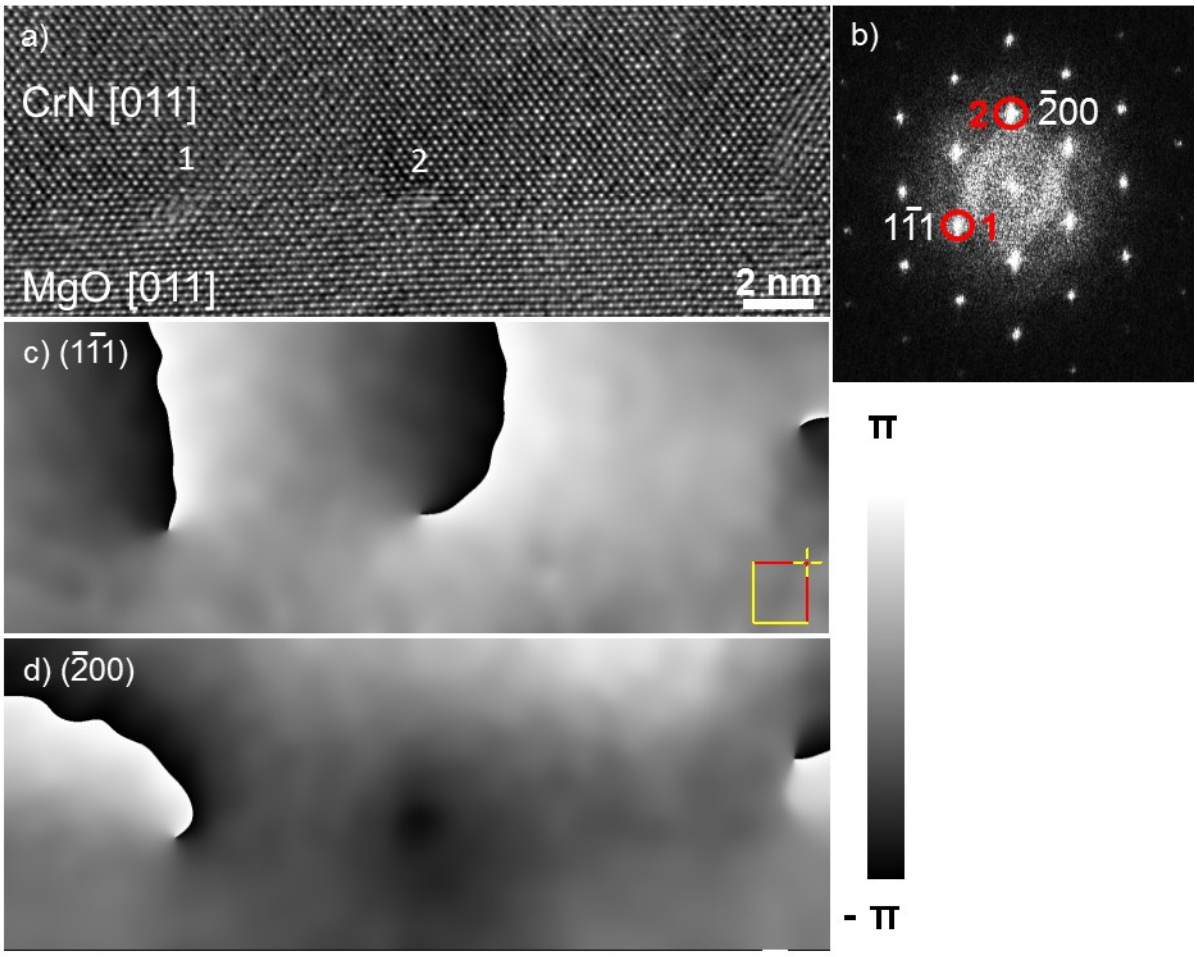

Figure 5.6: a) HRTEM image of CrN/MgO interface; b) power spectrum with selected reflections corresponding with c) phase image 1 and d) phase image 2; the color scale indicates phase changes from –π to +π.

The phase images of the $(\bar{2}00)$ and the $(1\bar{1}1)$ reflection were used to calculate a two dimensional relative strain map of Fig 5.7a. In Fig. 5.7b and c the relative strain maps in x- and y-direction are shown. The color scale indicates strain changes from –14.7% to +16.6%. The x-direction was taken parallel to the interface, the y-direction is normal to the interface. One can identify directly the exact positions of the dislocations. The relative strain maps in Fig. 5.7b and c exhibit that the strain is nearly constant in the

substrate and in the layer (because of constant color contrast). But the areas of the dislocation cores at the interface show strong distortions. An enlarged image of the dislocation core strain field of the pure edge dislocation is shown in Fig. 5.7f. The strain field is symmetrical and follows the contours of the number 8. Below the dislocation core in the MgO side an expanded region is apparent and a field of compression in the region of the extra half-plane in the CrN layer. The expanded area extends further into the CrN layer than the compressed region in the MgO substrate. In the exact core there is an abrupt change from the maximum compressive strain to maximum expansion strain. In y-direction the relative strain is zero for the pure edge dislocation (dislocation 2). Dislocation 1 (see Fig. 5.5b and 5.7c) exhibits a strain field in y-direction due to the extra (200) plane inserted parallel to the interface (see also Fig. 5.4e). A line profile across the interface (averaged over ~ 6.5 nm reaching from the CrN into the MgO substrate, see black rectangle in Fig. 5.7b) is drawn to visualize the relative strains. The relative strain distribution shows no strain in the substrate adjacent to the interface. At the interface and in the CrN layer the lattice is compressed due to the smaller lattice constant of CrN. The red dotted line marks the position of the interface (see Fig. 5.7b and Fig. 5.7e) determined by drawing a line through the dislocation core. This position may not coincide with the structural or chemical position of the interface but was used as a simple and reproducible criterion in this study.

An enlarged detail of the MgO substrate is shown in Fig. 5.7g. One can distinguish in this image between the magnesium and the oxygen atoms. The spots with a weaker intensity correspond to the O atoms, while the brighter spots belong to the Mg atoms. It was not possible to differ between chromium and nitrogen atoms in the HRTEM images, probably because of different atomic-scattering factors of the four atom species.

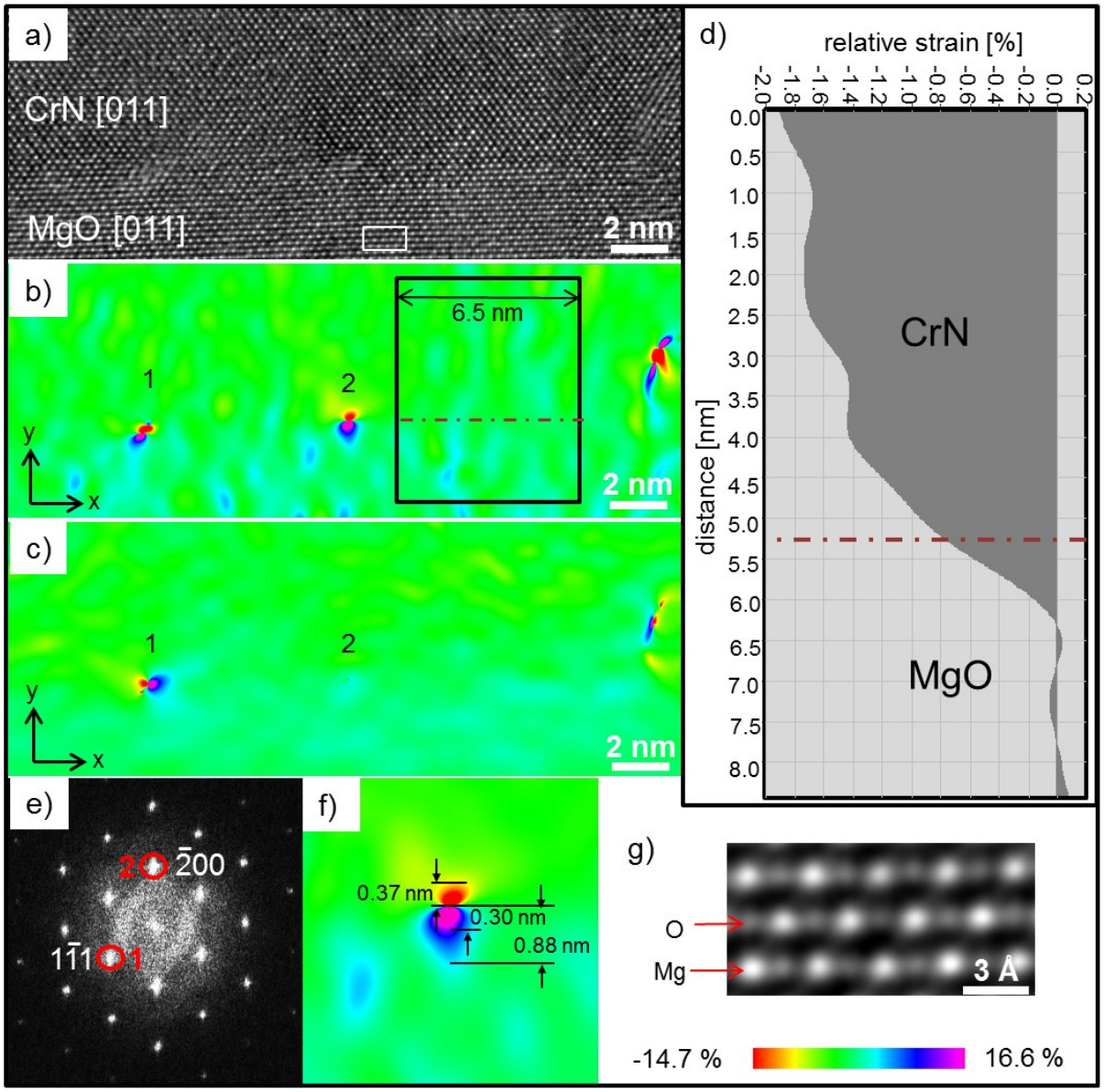

Figure 5.7: a) HRTEM image of CrN/MgO interface; b) relative strain map in x-direction of dislocation 1 and 2; c) relative strain map in y-direction of dislocation 1 and 2; d) line profile plot of the relative strain distribution in x-direction across the interface averaged over 6.5 nm (selected area see black rectangle); e) power spectrum with selected reflections; f) detail of the dislocation core.

5.2. Sample B: CrN single layer on MgO

For a detailed characterization of the CrN single layer plan-view and cross-sectional samples were prepared. The different perspectives are shown in the drawing in Fig. 5.8. In the plan-view sample (see green square) one can see a polycrystalline material; in the cross-section image (see orange square) the columnar structure of the layer is visible. The results of both samples are described below.

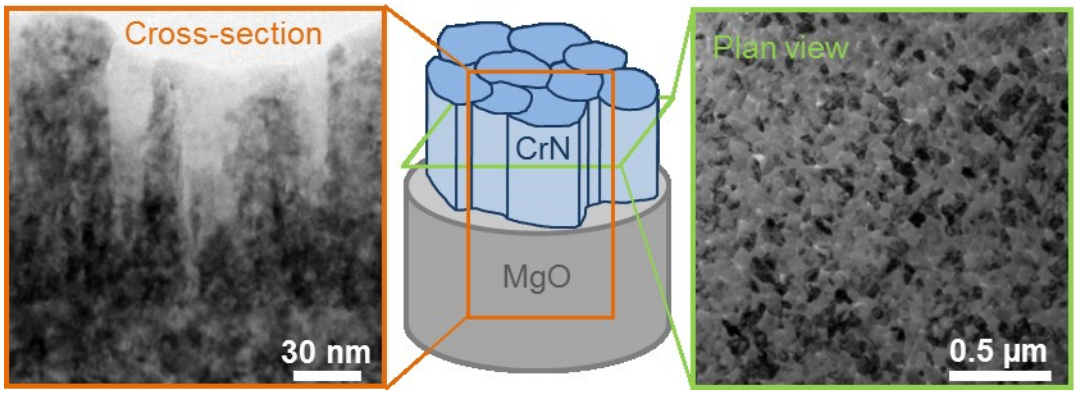

Figure 5.8: Schematic drawing of the CrN single layer on the MgO substrate with a cross-sectional TEM image provided in the orange rectangle and a plan-view image in the green rectangle.

5.2.1. Plan-view sample

Plan-view TEM studies revealed that the CrN film is polycrystalline (Fig. 5.9a). The corresponding diffraction pattern is shown in Fig. 5.9b. The rings are not of constant brightness (the image contrast in Fig. 5.9b is inverted); instead of rings only short arcs are observed. Hence the material has a texture: the reflections of the (111) and (220) planes are preferred. Contrary the ring associated with the (200) lattice planes is very weak. So the majority of the grains is oriented in $[1\bar{1}0]$ direction. In Fig 5.9c a detailed image of the grains and their shapes are apparent. The grains in Fig. 5.9a appear in dark and bright gray contrast, which could derive from the orientation contrast.

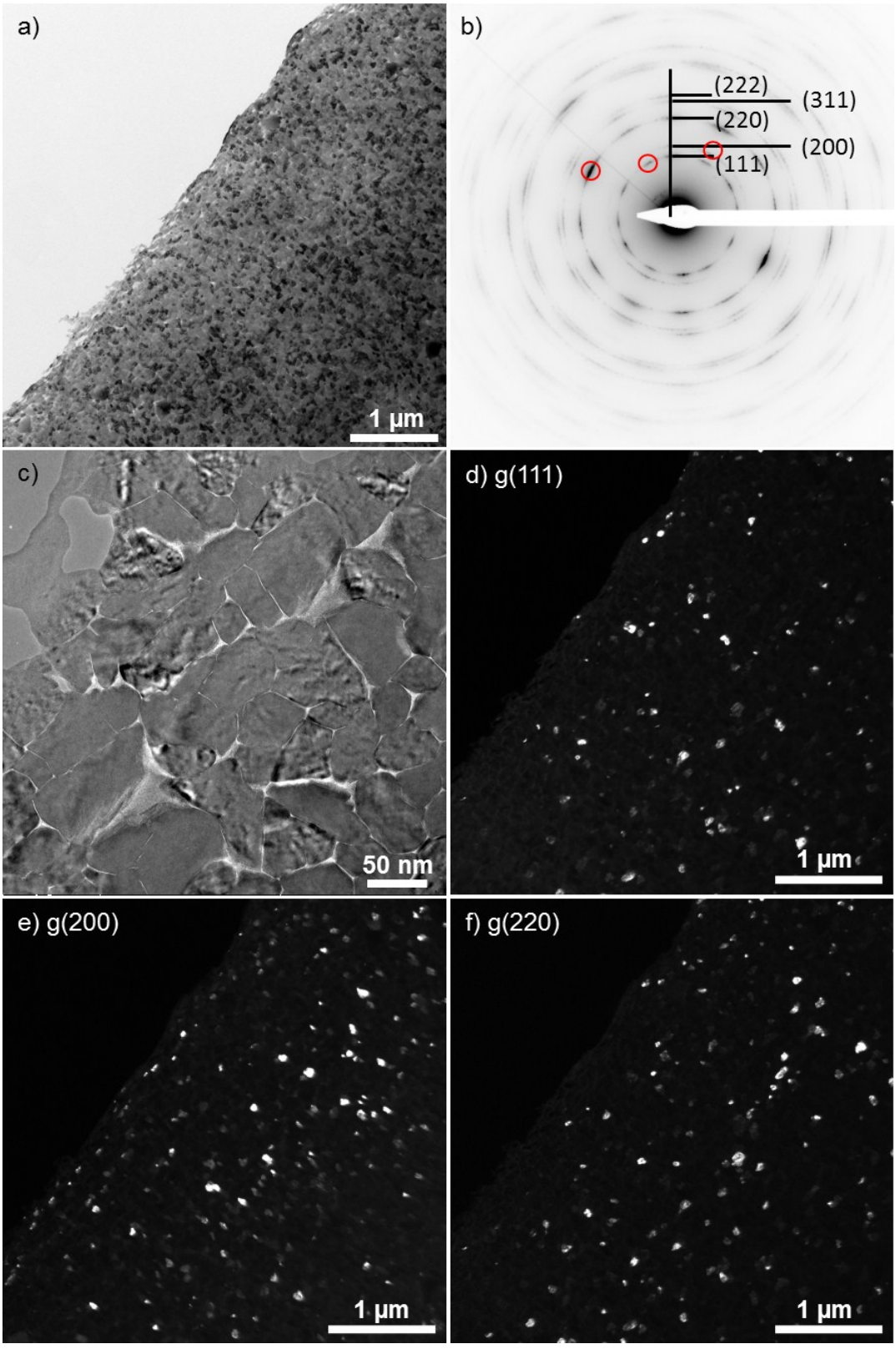

Figure 5.9: a) Plan-view BF image; b) SAD pattern with inverted contrast; c) detailed image; d) DF image using g(111); e) DF image using g(200); f) DF image using g(220).

In Fig. 5.9 d, e and f different parts of the ring pattern ($g_{(111)}$, $g_{(200)}$ and $g_{(220)}$ red encircled in Fig. 5.9b) were selected with the object aperture to create DF images. In the images the grains which satisfy the particular orientation are showing bright contrast. The DF images indicate that the grains are all in the same size range.

For a determination of the grain size distribution 110 grains were measured. The diagram in Fig. 5.10 shows that the most grains range between 35 and 60 nm in diameter.

On the basis of XEDS measurements the region were the MgO substrate was completely removed by ion milling was determined. Up to a distance of 700 nm away from the edge of the sample the film consists of pure chromium nitride.

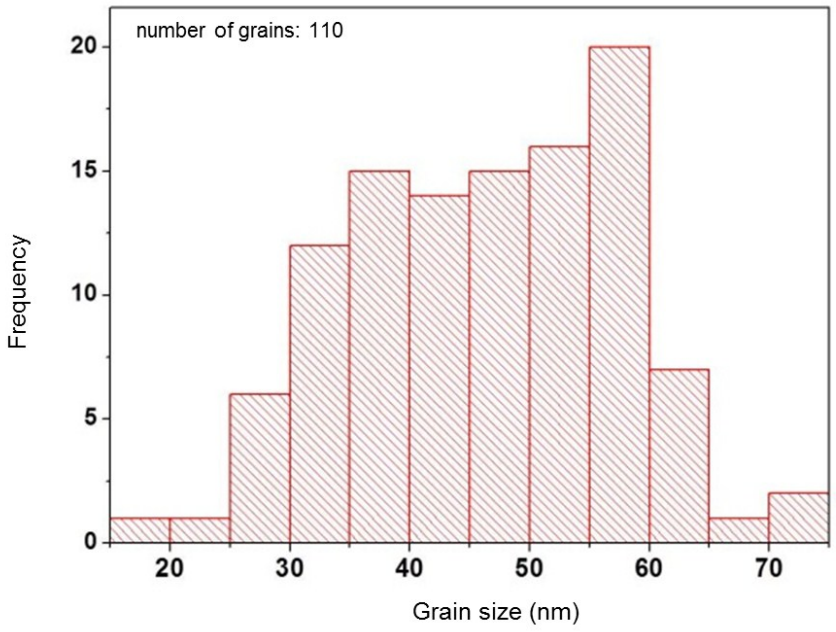

Figure 5.10: Grain size distribution of the CrN single layer (number of measured grains: 110).

5.2.2. Cross-sectional sample – Conventional TEM

The CrN single layer had a total thickness of more than 1 µm after the deposition process. Because of this thickness the film grows in a polycrystalline columnar manner, which is apparent in the BF image in Fig. 5.11a. The CrN region directly on top of the substrate shows a homogenous contrast. To determine the orientation of the CrN the substrate was tilted in [001] zone axis as seen in the SAD patterns in Fig. 5.11b. Four SAD patterns in different areas of the layer (the selected areas are encircled in Fig. 5.11a) have been recorded (see Fig. 5.11d, e and f). The diffraction pattern in Fig 5.12c indicates that the layer first grows single crystalline before the material forms polycrystalline columns. The SAD aperture had a size of 10 µm. Therefore the SAD patterns recorded in the polycrystalline CrN layer contain reflections from more than one column. The neighboring columns show slightly varying orientations near the single crystalline region as seen in the DP in Fig. 5.11d. Further away from the substrate the existing orientations are changing and the (111) reflections are getting stronger (see SAD patterns in Fig. 5.11e and f). A development of a texture from a preferred [001] growth direction to an orientation with favored (111) planes instead of (200) and (220) planes was obtained. A theoretical ring pattern for CrN is pictured in Fig. 5.11g. The mean column width was between 20 and 60 nm (see Fig. 5.12). The column diameters were measured along a line as indicated in Fig. 5.11a.

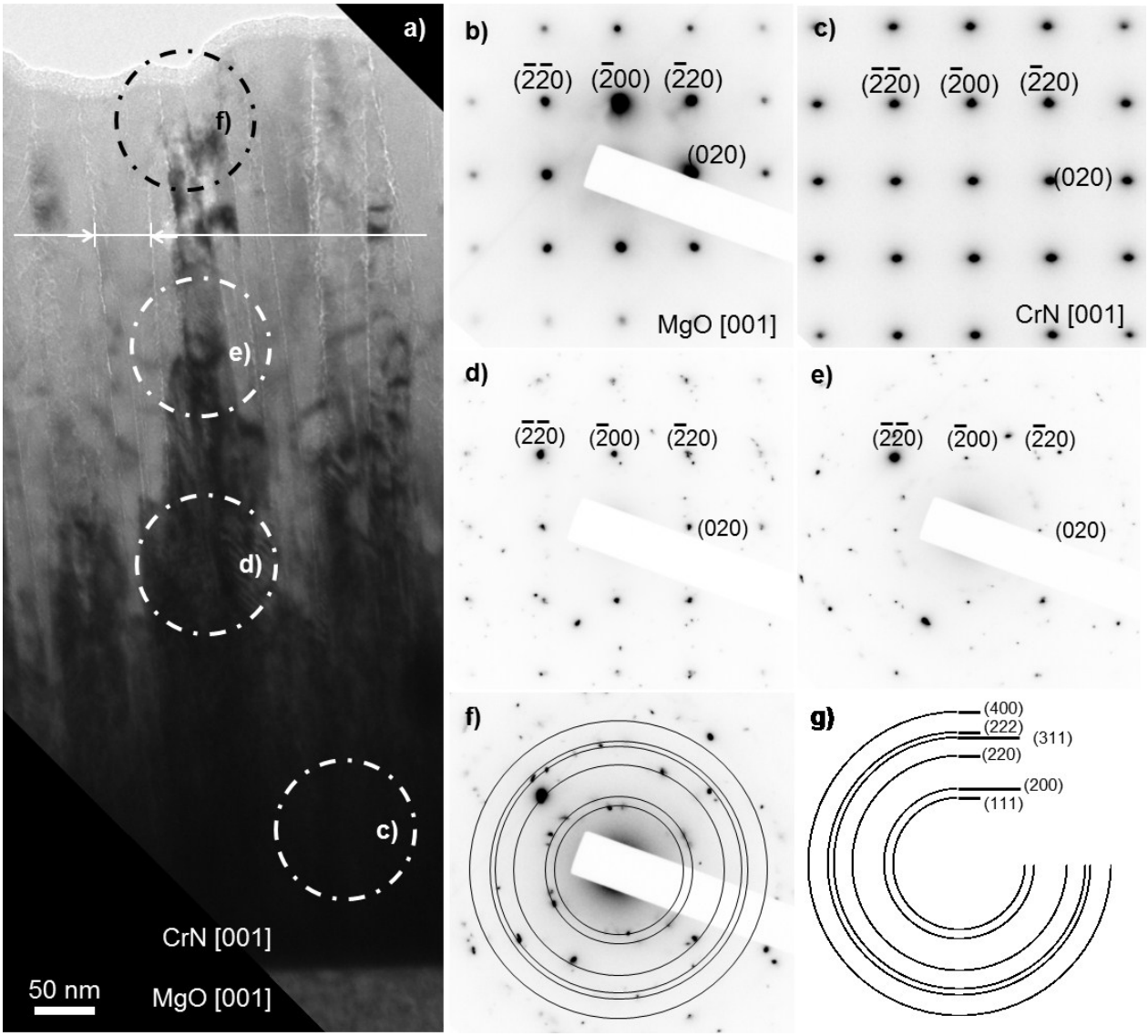

Figure 5.11: a) BF image of the CrN single layer; b) SAD of the MgO substrate; c) SAD of single crystalline CrN layer; d-f) SAD of columnar structured CrN layer; g) drawing of a CrN ring pattern; the selected areas for c–f) are indicated with circles in a).

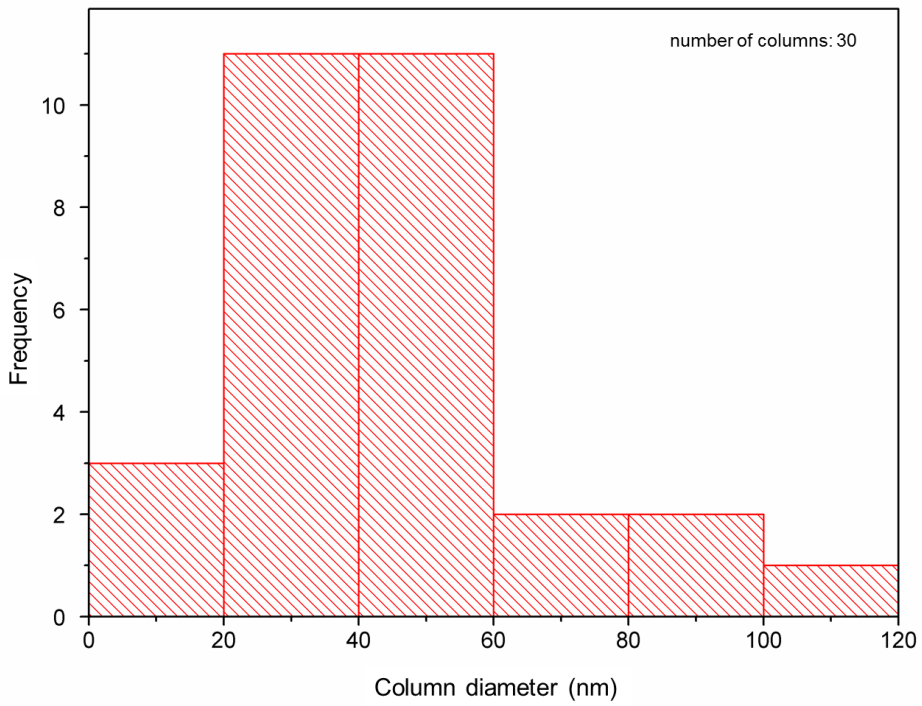

Figure 5.12: Grain size distribution of the CrN single layer (number of measured columns: 30).

5.2.3. Cross-sectional sample – HRTEM and GPA

The HRTEM image (see Fig. 5.13c) shows that the interface between CrN and MgO is not atomically flat. Additionally the presence of a lot of defects in the layer and the substrate is revealed. One can see that the layer grows epitaxial on the substrate. The position of the interface is indicated with a dot-dashed line. The approximately structural interface width indicated in Fig. 512a is about 1.5 nm. The roughness of the interface ranges over about 4 nm.

Three positions of dislocations at or near the interface are marked with arrows. The spacing between the misfit dislocations is about 10 nm. To visualize the dislocations and the additional planes a Bragg filtered image is shown in Fig. 5.12b. The extra (020) planes are clearly apparent and marked with arrows.

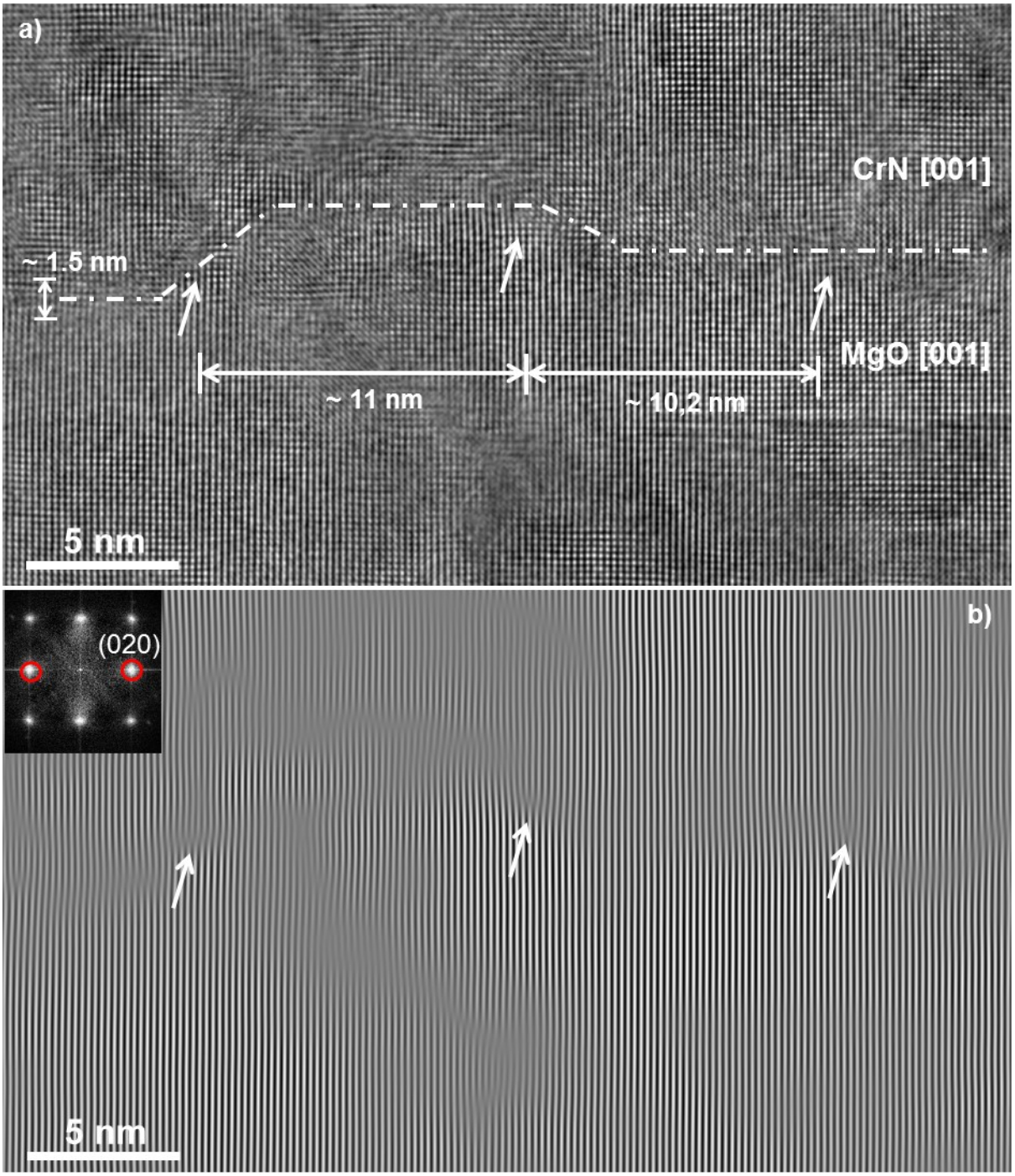

Figure 5.13: a) HRTEM image of the CrN/MgO interface; b) Bragg filtered image of a) using the red encircled reflections (see inset).

In Fig. 5.13 the central dislocation is imaged enlarged and a Burgers circuit is drawn. The white dots are at the atom positions. The resulting Burgers vector $\vec{b}$ = ½a_{CrN}<100>

is parallel to the interface and the dislocation is of pure edge type. The Bragg filtered image represents the (020) extra plane on the CrN side forming the misfit dislocation.

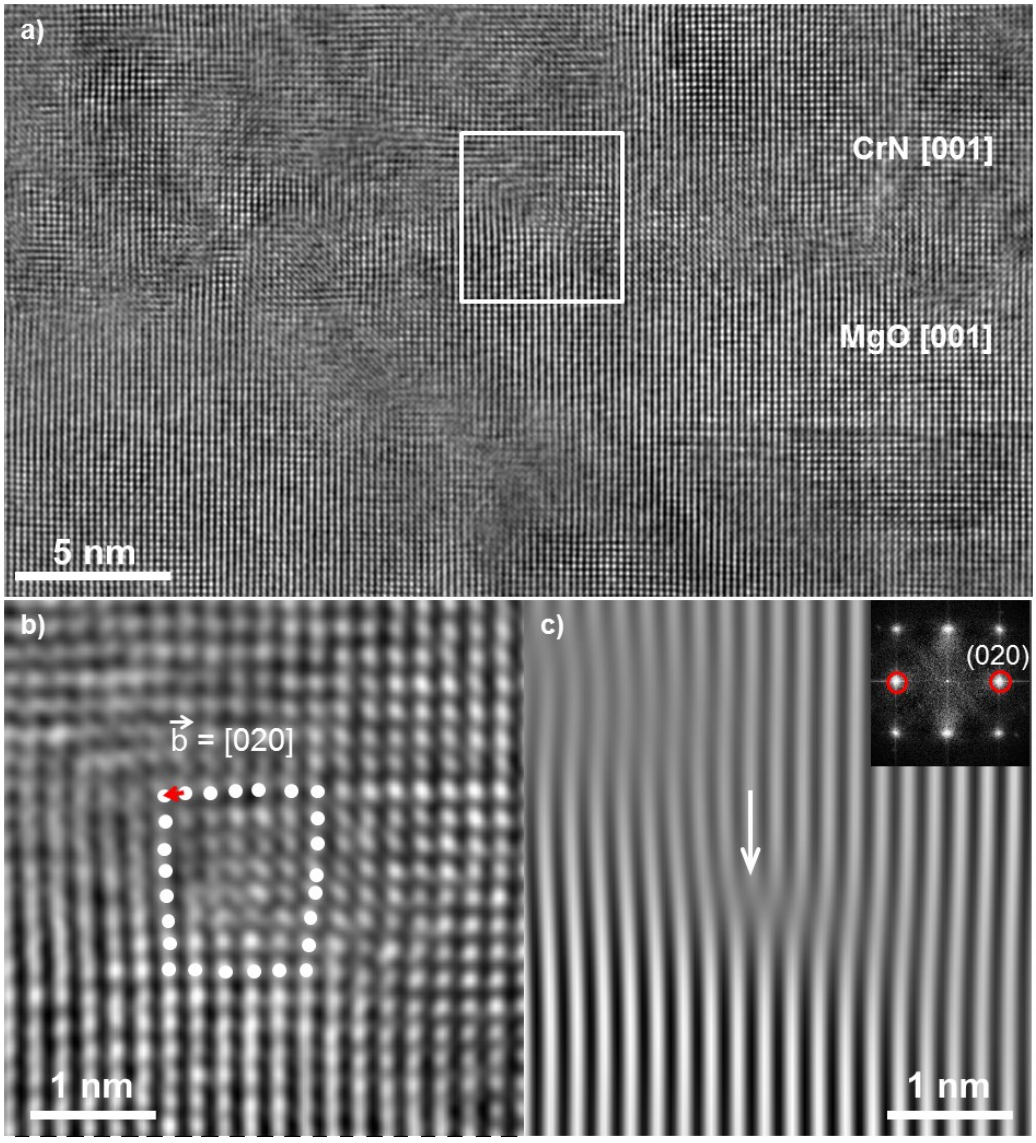

Figure 5.14: a) HRTEM image of CrN/MgO interface; b) detailed image of a dislocation with Burgers circuit and vector; c) Bragg filtered image of b) using a (020) reflection as indicated in the inserted FFT.

To visualize the deformations a relative strain map was calculated with GPA. The used spots are the $(0\bar{2}0)$ and the $(\bar{2}00)$ reflection (marked with circles in the power spectrum in Fig. 5.14d). The relative strain map in x-direction is shown in Fig 5.14b. A line profile was applied across the interface and averaged over a width of about 6.2 nm (see black

rectangle in Fig. 5.14b). The strain distribution illustrates that the strain in the MgO substrate, which was used as reference, is nearly zero. The CrN layer on the other hand is relatively compressed compared with the substrate due to a smaller lattice constant. In a range of 5 nm next to the interface the strain in the CrN layer is about 2.3%, further away from the interface the strain is decreasing again. The positions of the misfit dislocations (see also Fig. 5.12) are encircled. The strain map shows clearly strong deviations around the dislocation cores and the opposite expanded and compressed areas in the MgO and the CrN sides.

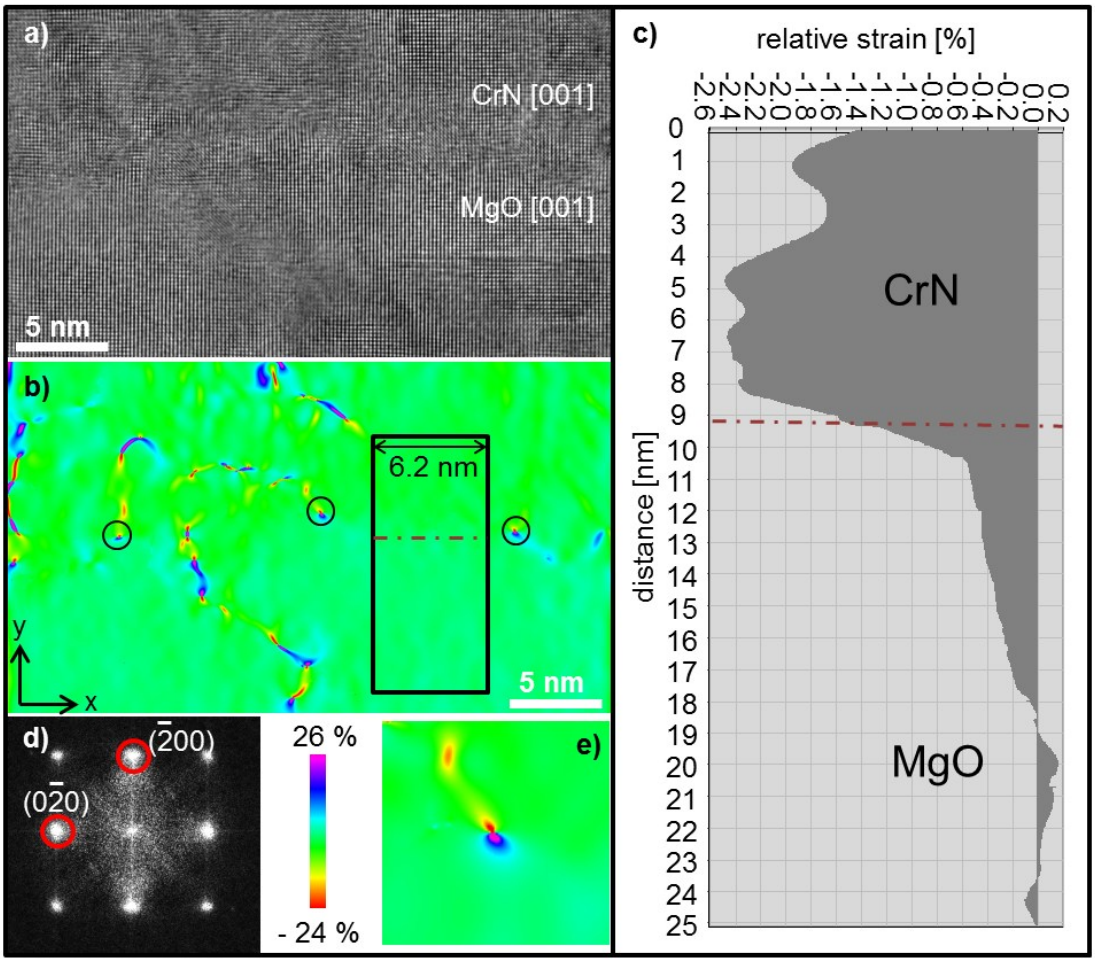

Figure 5.15: a) HRTEM image of CrN/MgO interface; b) relative strain map in x-direction of a); c) line scan plot of the relative strain distribution across the interface averaged over a width of 6.2 nm (selected area see rectangle in b)); d) power spectrum of a); selected reflections are encircled; e) enlarged detail of the centered dislocation.

5.2.4. Cross-sectional sample – EELS experiments

In order to analyze the chemical composition across the interface between the CrN layer and the MgO substrate EELS measurements were performed. It is essential to select very thin sample areas for the experiments. In Fig. 5.15a and b STEM-ADF and -HAADF images of the chosen region are shown. The relative thickness distribution along the line scan (see spectrum image in Fig. 5.15c) demonstrates that the sample is thin enough at this position ($t/\lambda < 0.6$). The line for the scan was applied at an angle of about 60° with respect to the interface. The step size was 0.75 nm, the probe size 0.2 nm. In this way more than 30 EEL core-loss and low-loss spectra have been recorded across the interface. The resulting data set of the core-loss spectra is shown in Fig. 5.16a.

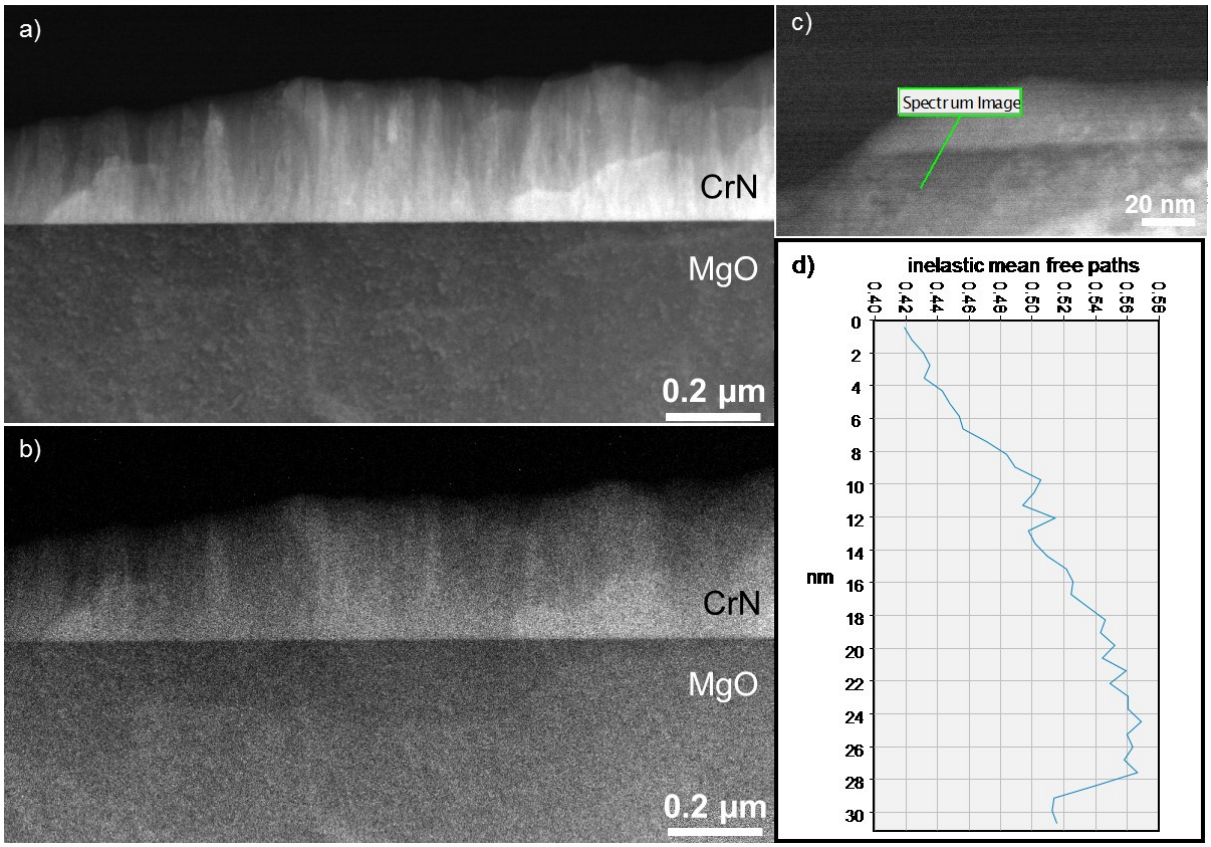

Figure 5.16: a) ADF-STEM image of the area chosen for EELS measurements; b) HAADF-STEM image of a); c) ADF-STEM image with applied line for EELS-scan; d) relative thickness distribution along the EELS line scan (computed with zero loss peaks).

Two extracted core-loss spectra of the CrN layer and the MgO substrate are shown in Fig. 5.16. The N-K edge appears at around 400 eV, the Cr-$L_{2,3}$ edge is at an energy loss of about 580 eV. The Mg-K edge is at the end of the spectrum at about 1300 eV, but the peak is not very distinctive. The O-K peak is positioned shortly before the Cr-$L_{2,3}$ edge at 550 eV. The relative tight distance between these two peaks and the weak Mg-K edge leads to difficulties in the quantification of the spectra. To separate the O-K and the Cr-$L_{2,3}$ edge the MLLS method was applied. Therefore, the two spectra shown in Fig. 5.16 were selected as reference spectra. The first spectrum (Fig. 5.16b) represents the CrN layer; the second spectrum (Fig. 5.16c) is representing the MgO substrate.

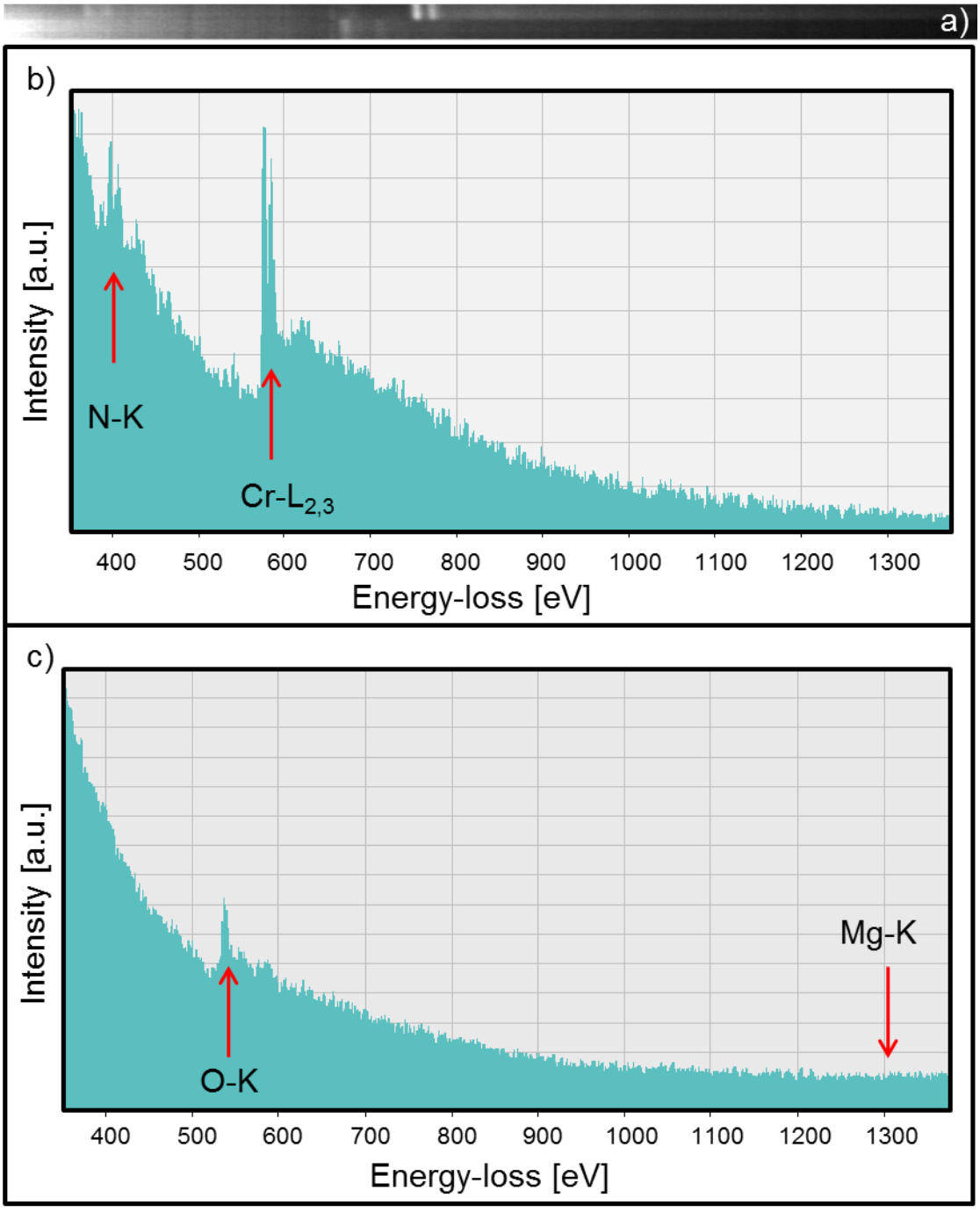

Figure 5.17: a) Spectrum image: core-loss data set (the right half of the set was cut out for a better view); b) EEL spectrum of CrN and c) EEL spectrum of MgO; characteristic edges are marked with arrows.

The MLLS algorithm calculates a model function that is a linear combination of these two reference spectra and fits that model to each spectrum in the data set. The deviation between the model and the selected spectra is minimized by regulating the coefficients of the linear terms. The result of the fitting process is now the optimum linear combination of the two reference spectra, thus the spatial distribution of them across the interface. From this fit-coefficient map one can see how much of the reference spectra is present in each spectrum of the data set. As seen in Fig. 5.17 until the first 10 nm in the line scan about 100% CrN is present. Between 10 nm and 15 nm the interface appears. The interface width was measured once from 100 % CrN to 100 % MgO, which lead to a width of 5 nm and once again from 75 % CrN to 25 % CrN with a resulting width of 2.1 nm. In consideration of an angle of 60° between line scan and interface the width is reduced to 4.3 nm in the first case and to 1.8 nm in the second case. After 15 nm nearly 100 % MgO is existent.

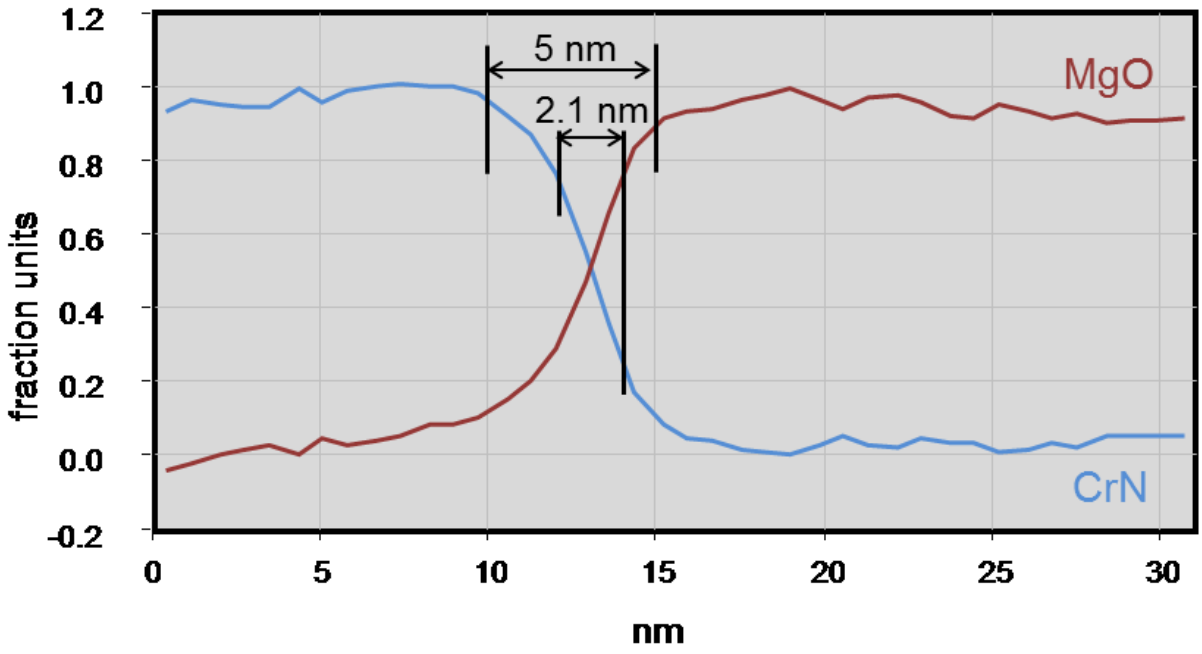

Figure 5.18: Fit-coefficient map: spatial distribution of CrN and MgO across the interface.

6. Discussion

6.1. Structural and orientation characterization

The fundamental structural characteristics have been investigated by conventional TEM investigations (see Fig. 5.1a, b and c). Based on contrast changes in conventional TEM and on intensity changes in ADF-STEM images in Fig. 5.2 the layer thickness of sample A was determined. Both measurements revealed a layer thickness of 10 nm for the CrN layer. The thickness of the Cr layer was about 18 nm in conventional TEM images and 13.5 nm in STEM images. The images were not calibrated, which could lead to the observed differences. Anyway, the measured thickness range is in good agreement with the requested sizes from the deposition process.

The orientation relationship between layers and substrate has been identified with SAD patterns. Both layers (A and B) showed the expected orientation relationships and in both samples the CrN layers grew epitaxial on the substrate. Just as the Cr film of sample A on the CrN film. The orientation relationship between the two layers in sample A is the following: Cr (100) ‖ CrN (100) and Cr [001] ‖ CrN [011]. On the other hand CrN grows in the same orientation as MgO, the orientation relationship between them is CrN (100) ‖ MgO (100) and CrN [001] ‖ MgO [001] for both samples A and B. CrN and MgO have both a fcc rock salt structure with slightly different lattice constants of a_{MgO} = 0.4215 nm [23] and a_{CrN} = 0.4148 nm [24]. The lattice mismatch δ can be calculated with:

$$\delta = \frac{a_{substrate} - a_{film}}{a_{substrate}}. \tag{6.1}$$

The lattice mismatch between MgO and CrN is therefore[24] about 1.59%. The Cr has a body-centered cubic (bcc) structure with a lattice constant of a_{Cr} = 0.2884 nm [25], which is much smaller than the CrN lattice constant. The atomic models for Cr and CrN are shown in Fig. 6.1. From the orientation relationship between the CrN and the Cr film one can derive that the growth direction of Cr lattice is rotated by 45° with respect to the CrN

growth axis (see top view in Fig. 6.1). For this reason the mismatch between the Cr and the CrN lattice is minimized. Considering that the Cr [110] plane is now parallel to the CrN [100] plane the lattice mismatch is about 3.24%. This cell growth assembling of Cr on CrN was shown by Romero et al. [8], and the same orientation relationship was reported for Cr film directly grown on an MgO substrate by Wang et al. [19].

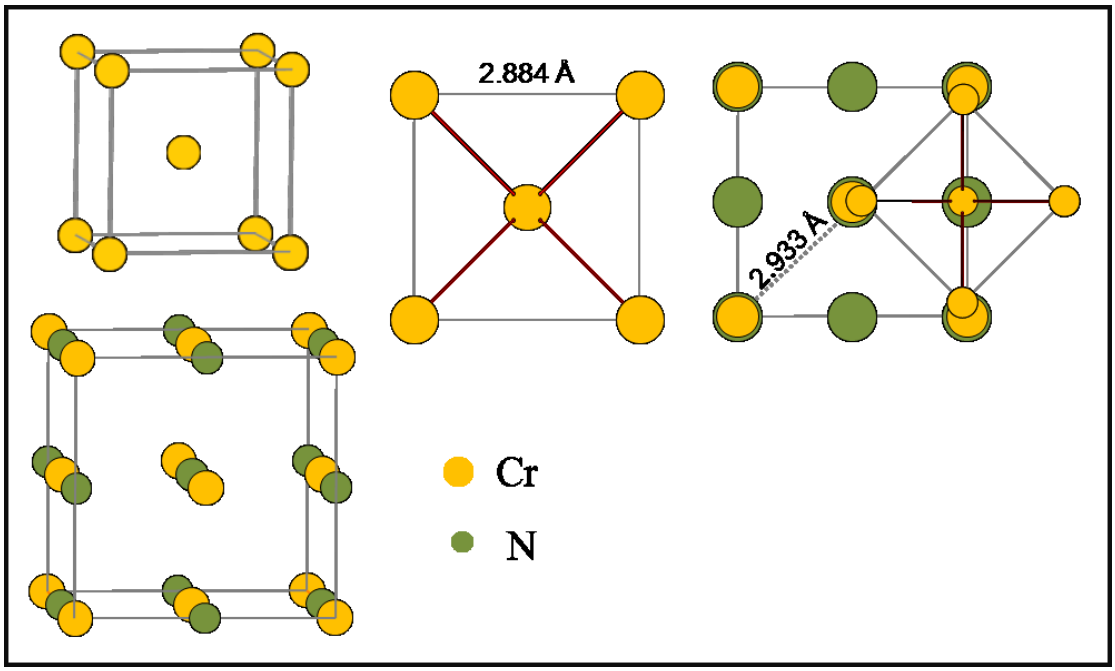

Figure 6.1: Atomic model for bcc Cr and fcc CrN and top view on cell growth of Cr on CrN.

In plan-view images (see Fig. 5.9) as well as in cross-section images (see Fig. 5.11) of the CrN single layer the regular shape and size of the grains respectively the columnar grains is evident. No extremely big grains have been observed. For the plan-view sample the grain size distribution in Fig. 5.10 showed that the most grains range between 35 and 60 nm in diameter. In the cross-sectional sample the column diameters were measured. The distribution (see Fig. 5.12) reveals that most crystals have a diameter between 20 and 60 nm, which is consistent with the values from the plan-view sample.

During the deposition process the CrN first nucleates single crystalline and epitaxially on the substrate, as seen in HRTEM images (Fig. 5.13a) and the growth direction is therefore the [001], which is predetermined by the substrate orientation. When the epitaxy cannot be sustained anymore a columnar polycrystalline structure is formed (see

Fig. 5.11a). This leads to small misorientations along these columnar grains and a change from the preferred [001] direction to other directions (for example [011]) in which the (111) reflections occur. The SAD patterns in Fig. 5.11 reveals slight changes in the orientation between neighboring grains. The ring pattern of the plan-view sample in Fig. 5.9b shows also a texture: the reflections from the (111) and (220) planes are stronger than the (200) ring. The [100] growth direction (perpendicular to the surface and along the columns) is thus replaced by a $[1\bar{1}0]$ growth direction.

A pronounced (111) texture of CrN films was also reported by Daniel et al. [26]. The investigated CrN layers had a thickness of about 3 µm and were grown on silicon substrates. They observed that in the beginning of the deposition process the (200) and (111) grains grow simultaneously until then the (111) grains are dominant and a nearly complete (111) texture is present. The condensation of particles on the surface depends on the growth kinetics, diffusion processes and surface reactions. The (200) planes are assembling with alternating Cr and N atoms. The (111) planes consist of monoatomic layers of either only chromium or only nitrogen atoms. Therefore the (200) planes are a high-potential energy planes, while the (111) are low-potential energy planes. The diffusion activity of Cr on (111) is very low; the incoming Cr atoms remain in stable positions on the N-terminated surface. On the other hand the N_2 molecules can dissociate when arriving on a surface occupied with Cr atoms. It was also shown that an increasing N_2 partial pressure from 0.25 to 0.75 Pa leads to a reversal of the growth direction, the (200) orientation is favored now because more N atoms are provided. Since the single layer sample in this thesis was deposited under very similar conditions (substrate temperature of 350 °C, layer thickness of more than 1 µm, bias voltage of - 40 V and a N_2 partial pressure of 0.25 Pa) it is obvious that the growth mechanism can be explained as described by Daniel et al.

Dislocation Analysis of the CrN/MgO interface

According to the O-lattice theory at {100} interfaces between two fcc crystals occur predominantly two kinds of dislocations networks: one with <110> dislocation line and a Burgers vector of $\vec{b}$=½a<$\bar{1}$10> and one with <100> dislocation lines and a Burgers vector of $\vec{b}$ = ½a<010> [27]. The equilibrium distance d between dislocation lines is determined by

$$d = \frac{|\vec{b}|}{\delta} \tag{6.2}$$

where $|\vec{b}|$ is the projected Burgers vector. The potential dislocation lines calculated with corresponding d-spacings are listed in table 6.1.

Table 6.1: D-spacings for different dislocation networks.

Viewing direction	Dislocation network	Projected Burgers vector [nm]	d-spacing [nm]
<110>	<100>	$\vec{b}$=½ a_{CrN} [110] = 0.2207	9.22
<110>	<110>	$\vec{b}$=½ a_{CrN} [100] = 0.3122	18.45
<100>	<100>	$\vec{b}$=½ a_{CrN} [100] = 0.2207	13.04

The generation of misfit dislocations along the interface between CrN and MgO has been shown for both samples in HRTEM images. In case of the bi-layer sample, the dislocation spacing was 7.5 nm (see Fig. 5.4a). As indicated in Fig 5.5c the projected Burgers vector for a pure edge dislocation is **b** = ½a [110]. According to F. Ernst [27] an end-on misfit dislocation in <100> projection tilted in <110> projection makes an angle of 45° with the projection direction. As seen in Fig 5.4 the angle between interface and inserted plane is 55°. The d-spacing of 7.5 nm is lower than the predicted values, but it is closer to 9.22 nm. It has to be noted that dislocation 1 (in Fig. 5.4-5.7) is not a pure edge dislocation and is therefore not a real misfit dislocation. In the single layer sample the misfit dislocations were oriented end-on in <100> direction. The d-spacing was about 10 nm, which is closer to 13.04 nm from the <100> dislocation network. So in both samples a <100> dislocation network is present.

Era et al. [17] investigated CrN layer deposited with varying N_2 partial pressure. They observed that with increasing N_2 pressure the crystal structure changes from hexagonal Cr_2N (at a nitrogen pressure of < 0.05 Pa) to a cubic CrN (at N_2 pressure of 0.105 Pa). And that the lattice parameter of the cubic CrN is increasing with increasing N_2 pressure. In this thesis no hexagonal Cr_2N was observed in any of the samples. But in the beginning of the deposition process the nitrogen pressure is possibly smaller than adjusted, which leads to a decreased lattice constant (because of a non-completely stoichiometric composition of CrN). This could be one reason for the higher dislocation density observed in both samples. Another reason could be a lattice damage caused by

the cooling of the sample from the substrate temperature (350°C). A higher dislocation density was also observed by Wang et al. [19] in Cr layers on MgO.

6.2. Geometric Phase Analysis

The GPA method was applied to HRTEM images of both samples. The technique exhibits strain and displacement fields at the interface and indicates very accurate positions of the misfit dislocations. The strain fields of dislocation cores of pure edge dislocations have been shown in detail in Fig. 5.7f for the bi-layer sample A and in Fig. 5.15f for the single layer sample B. In case of the sample A the strain field is symmetrical while in sample B the strain field of the central dislocation is distorted, but the others are also more symmetrical (see Fig. 5.15b). The symmetric shape also suggests an edge character for the dislocations. Additionally, in case of the pure edge dislocation the strain field in y-direction of sample A is almost not apparent. Such a symmetric figure-of-eight shape was also shown by *Zhao et al.* [28] for a pure edge dislocation in gold.

The relative strain maps reveal also some strong relative strained areas offside the interface due to defects from the deposition process. As seen in Fig.5 and in table 5.1 the CrN$(02\bar{2})$ lattice planes are about 1.73 % (± 0.04 %) compressed relative to the substrate, which nearly reflects the lattice mismatch between CrN and MgO of 1.59 %. The compression of the Cr lattice (3.52 % ± 0.16 %) is also in accordance with the lattice mismatch of 3.24 %. The line plot in the relative strain map of the CrN single layer exhibits that the region in the CrN layer next to the interface is more compressed (about 2.4 %) than in the region farther from the interface. In contrast the line profile in Fig 5.7b indicates an increase of the strain across the interface until a constant value of 1.8% is revealed.

6.3. Interface width of CrN/MgO

The interface between CrN and MgO is not atomically flat as observed in HRTEM images (see Fig. 5.3a for sample A and Fig. 5.12a for sample B). A structural interface width of 1.5 nm was observed from simple eye inspection for the single layer as indicated in Fig. 5.12a. The interfacial roughness of 1.5 nm is smaller than the chemical

intermixing obtained from EELS measurements (see Fig. 5.17), which was determined in two different ways. Considering that the interface is in the range of 100 % CrN and 100 % MgO the width is about 4.3 nm. Measuring from 75 % CrN to 25 % CrN the interface is about 1.8 nm wide. With low-angle XRD scans the interfacial roughness could be obtained [8].

7. Summary and Outlook

Chromium nitride is a very well investigated coating material. Nevertheless there is a need for further and detailed analysis to ensure a progress in material properties enhancement and improved deposition techniques. Therefore two samples have been investigated, one Cr(10 nm)/CrN(10 nm) bi-layer and one CrN(1 µm) single layer. Both layers were grown by unbalanced magnetron sputter deposition on MgO substrates. The orientation relationship for the CrN layer on MgO was determined as followed: CrN (100) ‖ MgO (100) and CrN [001] ‖ MgO [001] for both samples. The orientation relationship between Cr and CrN was Cr (100) ‖ CrN (100) and Cr [001] ‖ CrN [011]. The two layers of the bi-layer sample were grown single crystalline, the single layer formed a polycrystalline columnar structure, which was shown in cross-section as well as in plan-view samples. An evolution of preferred orientations along these columnar grains was observed: a change from an epitaxial grown single crystalline layer with a favored [001] orientation to a polycrystalline structure with occurring (111) planes.

The grain size distribution exhibits that the most grain range between 35 and 60 nm in diameter for the plan-view sample and a similar distribution was obtained for the cross-sectional sample, in which the measured column diameters ranged between 20 and 60 nm.

The microstructure at atomic level has been analyzed with HRTEM images. Both layers were grown epitaxial on the substrate and misfit dislocations in end-on orientation were found at the CrN/MgO interface. The dislocation spacing was in both cases lower than expected from theoretical calculations. The GPA technique was applied to HRTEM images. Two-dimensional relative strain maps exhibited the strain field around dislocation cores. A symmetric strain field was observed for some pure edge dislocations.

EEL spectra were recorded for the CrN single layer in 0.75 nm steps across the interface. A spatial distribution of CrN and MgO has been shown and the interface width was determined in different ways. An attempt to demonstrate elemental evolution at the interface was not successful.

To get more detailed information of the chemistry at the CrN/MgO interface, the EELS data has to be processed with other fitting techniques. Additional measurements,

possibly in combination with heating experiments, can help to understand constitution and behavior of the layer. The effect of electron irradiation on the configuration is another interesting potential experiment.

To investigate the changes in orientations along the columnar grains nano beam diffraction experiments can be done. For a better determination of the occurring misfit dislocation network of the bi- layer sample, the interface could also be visualized in [001] viewing direction. Altogether, plenty of experiments can be done to get a fundamental understanding of the extraordinary properties of CrN films and their interaction with substrate materials.

References

[1] P. Panjan, “Industrial applications of CrN (PVD) coatings, deposited at high and low temperatures,” *Surface and Coatings Technology*, vol. 97, pp. 182-191, 1997.

[2] P. Wiecinski, J. Smolik, H. Garbacz, and K. J. Kurzydlowski, “Microstructure and mechanical properties of nanostructure multilayer CrN/Cr coatings on titanium alloy,” *Thin Solid Films*, vol. 519, no. 12, pp. 4069-4073, Apr. 2011.

[3] M. Kot, W. Rakowski, L. Major, R. Major, and J. Morgiel, “Effect of bilayer period on properties of Cr/CrN multilayer coatings produced by laser ablation,” *Surface and Coatings Technology*, vol. 202, no. 15, pp. 3501-3506, Apr. 2008.

[4] K. Rzepiejewska-Malyska, M. Parlinska-Wojtan, K. Wasmer, K. Hejduk, and J. Michler, “In-situ SEM indentation studies of the deformation mechanisms in TiN, CrN and TiN/CrN,” *Micron*, vol. 40, pp. 22-27, 2009.

[5] L. Major, W. Tirry, and G. Van Tendeloo, “Microstructure and defect characterization at interfaces in TiN/CrN multilayer coatings,” *Surface & Coatings Technology*, vol. 202, pp. 6075-6080, 2008.

[6] X. Y. Zhang and D. Gall, “CrN electronic structure and vibrational modes : An optical analysis,” *Physical Review B*, pp. 1-9, 2010.

[7] X. Y. Zhang and D. Gall, “Surface mound formation during epitaxial growth of CrN(001),” *Thin Solid Films*, vol. 518, no. 14, pp. 3813-3818, May. 2010.

[8] J. Romero, J. Esteve, and A. Lousa, “Period dependence of hardness and microstructure on nanometric Cr/CrN multilayers,” *Surface and Coatings Technology*, vol. 188-189, pp. 338-343, Nov. 2004.

[9] J. W. Seok, N. M. Jadeed, and R. Y. Lin, “Sputter-deposited nanocrystalline Cr and CrN coatings on steels,” *Surface & Coatings Technology*, vol. 138, pp. 14-22, 2001.

[10] W. Carter, *Transmission Electron Microscopy*, Second. Springer US, 2009, p. 760.

[11] M. von Heimendahl, *Einführung in die Elektronenmikroskopie*. Karlsruhe und Stuttgart: Macherauch, E.; Gerold V., 1970, p. 195.

[12] M.J. Hÿtch, “GEOMETRIC PHASE ANALYSIS OF HIGH RESOLUTION ELECTRON MICROSCOPE IMAGES,” *Scanning Microscopy*, vol. 11, pp. 53-66, 1997.

[13] M. J. Hÿtch, E. Snoeck, and R. Kilaas, “Quantitative measurement of displacement and strain fields from HREM micrographs,” *Ultramicroscopy*, vol. 74, pp. 131-146, 1998.

[14] A. Maigne, “How to optimize your EELS experiments by adjusting the collection angle of your spectrometer?,” 2008. [Online]. Available: http://gatan.com/resources/knowhow/kh19_eels.php. [Accessed: 22-Feb-2012].

[15] R. F. Egerton, *Electron energy-loss spectroscopy in the electron microscope*, 2nd ed. New York, NY: plenum press, 1996, p. 485.

[16] C. Mitterbauer, C. Hebert, G. Kothleitner, F. Hofer, P. Schattschneider, and H. W. Zandbergen, “Electron energy loss-near edge structure as a fingerprint for identifying chromium nitrides,” *Solid State Communications*, vol. 130, pp. 209-213, 2004.

[17] H. Era, Y. Ide, A. Nino, and K. Kishitake, “TEM study on chromium nitride coatings deposited by reactive sputter method,” *Surface & Coatings Technology*, vol. 194, pp. 265 - 270, 2005.

[18] S. Han et al., “The effect of Cr interlayer on the microstructure of CrN coatings on steel,” *Thin Solid Films*, vol. 377-378, pp. 578-584, 2000.

[19] C. Wang, T. C. Kaspar, V. Shutthanandan, A. G. Joly, and R. J. Kurtz, “Structure of Cr film epitaxially grown on MgO (0 0 1),” *Acta Materialia*, vol. 59, no. 11, pp. 4274-4282, 2011.

[20] S. Cazottes, Z. L. Zhang, R. Daniel, J. S. Chawla, D. Gall, and G. Dehm, “Structural characterization of a Cu/MgO(001) interface using CS-corrected HRTEM,” *Thin Solid Films*, vol. 519, no. 5, pp. 1662-1667, Dec. 2010.

[21] C. Mitterbauer, W. Grogger, P. Wilhartitz, and F. Hofer, “Electron-irradiation damage in chromium nitrides and chromium oxynitride thin films.” *Micron*, vol. 37, no. 5, pp. 385-388, Jan. 2006.

[22] A. Strecker, U. Salzberger, and J. Mayer, “Specimen preparation for transmission electron microscopy(TEM)-reliable method for cross sections and brittle materials,” *Prakt. Metallogr.*, vol. 30, p. 482, 1993.

[23] J. Zhao, L. Lu, X. Chen, and Y. Bai, “First-principles calculations for elastic properties of the rocksalt structure MgO,” *Physica B*, vol. 387, pp. 245-249, 2007.

[24] M. R. and J. P. N. Eddine, E. F. Bertaut, “Etude cristallographique de Cr1-xVxN à basse temperature,” *Acta Cryst.*, vol. 33, pp. 3010-3013, 1977.

[25] H. E. Swanson, N. T. Gilfrich, and UgrinicG.M., “Standard X-Ray diffraction powder patterns,” *National Bureau of Standards (U.S.)*, vol. 539, no. 5, pp. 1-75, 1955.

[26] R. Daniel, K. J. Martinschitz, J. Keckes, and C. Mitterer, “Texture development in polycrystalline CrN coatings: the role of growth conditions and a Cr interlayer,” *Journal of Physics D: Applied Physics*, vol. 42, no. 7, p. 075401, Apr. 2009.

[27] F. Ernst, “Metal-oxide interfaces,” *Materials Science and Engineering*, vol. 14, pp. 97-156, 1995.

[28] C. W. Zhao, Y. M. Xing, C. E. Zhou, and P. C. Bai, “Experimental examination of displacement and strain fields in an edge dislocation core,” *Acta Materialia*, vol. 56, pp. 2570-2575, 2008.

List of Figures

List of Tables

List of Abbreviations

ADF	Annular Dark Field
bcc	body-centered cubic
BF	Bright Field
CCD	Charge-coupled Device
CVD	Chemical Vapor Deposition
DF	Dark Field
EELS	Electron Energy-Loss Spectroscopy
ELNES	Energy-Loss Near-Edge Structure
EXELFS	Extended Energy-Loss Fine Structure
fcc	face-centered cubic
FIB	Focus Ion Beam
FFT	Fast Fourier Transform
hcp	hexagonal closest packed
HAADF	High Angle Annular Dark Field
HRTEM	High Resolution TEM
GPA	Geometric Phase Analysis
MLLS	Multiple Linear Least Squares
PAPVD	Plasma Assisted PVD
PVD	Physical Vapor Deposition
ROI	Region of Interest
SAD	Selected Area Diffraction
SEM	Scanning Electron microscopy
STEM	Scanning Transmission Electron Microscopy
TEM	Transmission Electron Microscopy
WBDF	Weak Beam Dark Field

XEDS	X-Ray Energy Dispersive Spectroscopy
XRD	X-Ray Diffraction
ZLP	Zero Loss Peak
Å	Angstrom (10^{-10} m)
a	lattice constant
$\vec{a}$	real space lattice vector
α	convergence semi-angle
β	collection semi-angle
A_g	Amplitude of H_g
$\vec{b}$	Burgers vector
d	equilibrium distance between misfit dislocations
δ	lattice mismatch
e	gradient of the displacement field
eV	electron-volt
ε	strain field
$\vec{g}$	Bragg periodicity
Pa	Pascal
H_g	Fourier component of **g**
I	Intensity
λ	inelastic mean free path
Λ	bilayer period
µm	micrometer (10^{-6} m)
ms	millisecond (10^{-3} s)
N	Newton (kg·m/s^2)
nm	nanometer (10^{-9} m)
P_g	Phase of H_g

$\boldsymbol{r}$	position vector
rad	radiant
s	second
t	specimen thickness
$\boldsymbol{u}$	displacement field
V	Volt
W	Watt
°	degree
°C	degree Celsius